https://doi.org/10.5194/egusphere-2026-3679
Preprint. Discussion started: 20 July 2026
© Author(s) 2026. CC BY 4.0 License.

Complementarity between Large-Eddy Simulation and Synthetic-Aperture Radar observations to characterise surface wind in an extratropical cyclone

Nicolas Maury[1], Florian Pantillon[1], Sophia E. Brumer[1], Joris Pianezze[1], Aurélien Colin[2], Romain Husson[2], and Alexis Mouche[3]

[1]LAERO, University of Toulouse, CNRS, IRD, Toulouse, France
[2]Collecte Localisation Satellite, Brest, France
[3]IFREMER, Université Brest, CNRS, IRD, Laboratoire d'Océanographie Physique et Spatiale, Brest, France

Correspondence: Nicolas Maury (nicolas.maury4@utoulouse.fr)

Abstract.

While the large-scale dynamics of extratropical cyclones are well understood, the mechanisms by which fine-scale processes generate strong surface winds remain poorly understood. Storm Alex, located over the English Channel on 2 October 2020, featured a secluded warm front associated with enhanced surface wind speeds. Its fine-scale structure is investigated using Synthetic Aperture Radar (SAR) observations and three Meso-NH Large-Eddy Simulations (LES), with spectral and two-dimensional auto-correlation analyses applied to both SAR data and LES outputs. The results reveal energetic fine-scale structures responsible for locally enhanced surface wind in three high wind speed regions identified from SAR data. These fine-scale structures are wind streaks quasi-aligned along the mean wind direction, with a characteristic length scale of approximately 1 km, about twice the marine boundary layer height. They are reproduced by LES in two of the three regions, where they are due to the presence of boundary layer rolls in which the strongest surface winds are associated with downward transport of momentum from a low-level jet. In the third region, the absence of boundary layer rolls in LES may be related either to insufficient thermal instability or to excessively strong simulated wind shear, suggesting a strong sensitivity to surface fluxes and vertical stability for developing boundary layer rolls within extratropical cyclones. Overall, this study demonstrates that combining LES and SAR observations provides a robust framework for accurately capturing, validating, and improving our understanding of the fine-scale processes associated with surface wind in an extratropical cyclone.

KEYWORDS: Extratropical cyclone; Synthetic Aperture Radar; Large-Eddy Simulations; Boundary layer Rolls

1 Introduction

Extratropical cyclones are among the main drivers of atmospheric variability in mid-latitudes, where they play a key role in the horizontal and vertical transport of heat and moisture. These low-pressure systems can be characterised by strong horizontal pressure gradients and generate intense winds, impacting human life and activities. In Europe, the majority of extratropical cyclones are formed in the North Atlantic during the boreal winter, where the confluence of warm air masses from the subtropics

© Author(s) 2026. CC BY 4.0 License.

and cold air masses from polar regions cause baroclinic instability. In a predominantly westward flow, they can rapidly deepen, particularly when interacting with the jet stream, and sometimes become meteorological bombs (Sanders and Gyakum, 1980). On landfall, their average surface winds can exceed 25 $\mathrm{m\,s^{-1}}$ (storm threshold in the Beaufort scale) and they can also cause heavy precipitation (Hobbs, 1978).

Once baroclinic instability leads to the formation of a low-pressure system, the surrounding air starts rotating in a cyclonic direction and the central pressure decreases. In this cyclonic vortex, fronts form at the interface between air masses. A distinction is made between warm fronts, in which warm air slides over cold air, causing continuous low rainfall following the formation of stratiform clouds, and cold fronts, in which cold air forces warm air upward. Cold fronts can trigger the formation of convective cells, with heavy precipitation and potentially intense wind gusts (Shapiro and Keyser, 1990). Associated with the frontal system, two main airstreams can be distinguished: the Warm Conveyor Belt (WCB) ahead of the cold front and the Cold Conveyor Belt (CCB) ahead of the warm front (Browning, 1990; Martínez-Alvarado et al., 2018). The WCB is a relatively warm and moist airstream that typically originates in the boundary layer and slowly ascends. In contrast, the CCB is located at lower levels, typically between the surface and about 2 km altitude. This airstream transports relatively cold air and usually flows westward. A low-level jet (LLJ) may develop within the CCB (Carlson, 1980; Browning, 1990; Lfarh et al., 2023; Gentile and Gray, 2023) and the WCB (Hewson and Neu, 2015; Blanchard et al., 2020), with wind speeds exceeding 25 $\mathrm{m\,s^{-1}}$, contributing to strong surface winds. High surface winds can also be formed by a descent of air from the frontal cloud head called a sting jet (Browning and Field, 2004; Eisenstein et al., 2020; Brumer et al., Submitted) or from the upper troposphere called a dry intrusion (Raveh-Rubin, 2017).

While the development mechanisms of extratropical cyclones are relatively well understood (Shapiro et al., 1999; Browning et al., 2000; Neu et al., 2013; Schultz et al., 2019), the formation of strong winds remains less explored, particularly regarding the intensity and spatial distribution of surface wind gusts. Recent numerical studies (Rivière et al., 2020; Pantillon et al., 2020; Lfarh et al., 2023) highlight the importance of boundary layer structures in surface wind speed formation, in particular the role of atmospheric rolls allowing a non-local transport of momentum in LLJs towards the surface in the subsiding branches. These numerical studies also suggest that these rolls have a large spectrum of horizontal lengthscales from less than 1 km to 10 km. Since some boundary rolls are about a kilometre wide, numerical weather prediction models are limited by their horizontal grid spacing of at least 1 km to explicitly resolve the roll circulations. The use of higher-resolution Large-Eddy Simulation (LES) becomes essential thanks to their ability to resolve the most energetic turbulent eddies in the atmosphere. Lfarh et al. (2023) demonstrates that a horizontal grid spacing of at most 200 m (an effective resolution of 800 m) is required to reproduce boundary layer rolls in an extratropical cyclone. In a tropical cyclone study, Li et al. (2021) similarly shows that a horizontal grid spacing of 100 m improves wind prediction through the explicit representation of rolls. In addition, such high resolutions provide a better match with the boundary layer wind observations.

In most LES studies, the lack of observational data limits the evaluation of results, both with respect to the characteristics of the boundary-layer structures and their role in wind transport. Ground-based wind profilers can provide a two-dimensional (z,t) indication of the presence of boundary layer rolls and extratropical cyclone wind speeds (Parton et al., 2009, 2010). Also, Doppler cloud radar observations presented in Browning et al. (2015) shows that LLJs can interact with boundary-layer

https://doi.org/10.5194/egusphere-2026-3679
Preprint. Discussion started: 20 July 2026
© Author(s) 2026. CC BY 4.0 License.

circulations and showers originating from higher-level clouds, potentially transporting the LLJ downward through precipitation. However, Doppler cloud radar observations are only available when clouds and/or precipitation provide sufficient scatterers. Ground-based Doppler lidars provide high-resolution representations of the vertical wind profile (Pantillon et al., 2020), with fine temporal resolution. However, they do not offer horizontal extension required to fully characterise the three-dimensional structure of the boundary layer. In addition, the wind detection disappears in the presence of clouds, which can hinder the characterisation of the LLJ, often located within or above boundary-layer cloud layers. The spatial coverage of such instruments is relatively sparse, unevenly distributed geographically, and predominantly at fixes locations. As a result, measurements are limited, since extratropical cyclones must pass directly overhead to be observed. Moreover, due to the practical difficulties involved in deploying them during field campaigns, offshore extratropical cyclones are not captured by these measurements.

To address this lack of data, scatterometers in C-band from low-orbit satellites in sun-synchronous orbit have been used to characterise wind speed over ocean with their large swath (≈ 500 km). ASCAT (Advanced Scatterometer, Figa-Saldana et al. (2002)) carried onboard the Meteorological Operational (MetOp) polar satellites has been used to investigate surface wind dynamics in extratropical cyclones (Pineau-Guillou et al., 2018) but the coarse spatial resolution (~ 10 km) and long revisit time (~ 12 h) remain a limitation for hazard studies. Moreover, the accuracy is reduced at high wind speed (Chou et al., 2013). To increase the observational resolution in open sea, Sentinel 1 constellation satellites (Sentinel-1 A, B, C and D) are a source of valuable information thanks to their C-band Synthetic Aperture Radar (SAR) with spatial resolution between 20 m and 100 m. The ability to perform wind retrieval from SAR has been proven under high wind conditions (Mouche et al., 2017, 2019) and with fine horizontal resolution of ≈ 1 km and less. Over the past decades, SAR measurements have been extensively used to investigate sea surface winds (Mourad et al., 2000; Vandemark et al., 2001; Kudryavtsev et al., 2005; Ayet et al., 2021). Furthermore, the footprints on sea allow to determine atmospheric-oceanic interactions and processes, especially rolls in unstable marine boundary layers (Thompson et al., 1983; Alpers and Brümmer, 1994; Levy, 2001; Sikora and Ufermann, 2004; Wang et al., 2019, 2020; Granero Belinchon et al., 2022; Stopa et al., 2022) and in tropical cyclones (Zhang et al., 2008; Foster, 2013; Huang et al., 2018; Wang et al., 2018).

Although the ability to accurately detect low-pressure systems from SAR observations has been demonstrated (Fu, 1982; Young et al., 2002), these observations have not yet been compared with simulations of extratropical cyclones with comparable resolution. Furthermore, as highlighted by Lfarh et al. (2023), the interactions between mesoscale structures and boundary-layer circulations remain poorly understood from observational studies. The objectives of this study are (i) to evaluate LES of fine-scale phenomena using SAR observations and (ii) to interpret SAR surface signatures observations using LES within extratropical cyclones. This complementarity ultimately contributes to a better understanding of how boundary-layer circulations influence surface winds. To compare LES and SAR observations of an extratropical cyclone, the present case study focuses on Storm Alex (also named Brigitte by the FU Berlin), which formed on September 30th, 2020 in the Atlantic Ocean before making landfall in the evening of October 1st in French Brittany. This explosive extratropical cyclone (deepening of ≈ 40 hPa in 24 h) generated intense winds gusts exceeding 45 $\mathrm{m\,s^{-1}}$ on north-western French coasts and 25 $\mathrm{m\,s^{-1}}$ over land. Brumer et al. (Submitted), using Lagrangian trajectories, show that boundary-layer winds just prior to Alex's landfall are largely caused by a LLJ related to the CCB, as well as two further mesoscale airstreams, a sting jet and a dry intrusion. Storm Alex also caused

https://doi.org/10.5194/egusphere-2026-3679
Preprint. Discussion started: 20 July 2026
© Author(s) 2026. CC BY 4.0 License.

devastating floods in south-eastern France and north-western Italy (Ginesta et al., 2024; Martins et al., 2024). After crossing Brittany, Storm Alex remained over the Channel on October 2nd before returning to Brittany. Sentinel-1B passed over the windstorm at 6:23 UTC and captured the entire cyclonic system at a time when surface winds were exceeding 25 $\mathrm{m\,s^{-1}}$ along the coastal weather stations in the Channel. This unique opportunity enabled a comprehensive SAR–LES comparison across the entire system.

The article is organised as follows: Section 2 describes the various observations available, the numerical configuration and the diagnostics used to characterise Storm Alex. Section 3 focuses on the description of Storm Alex's mesoscale structures using satellite and ground-based observations, complemented by numerical simulations. Section 4 presents the results of three LESs in high-wind speed areas, compared with SAR data, with a focus on boundary-layer structures affecting surface winds. Section 5 summarises and analyses the results, and highlights the benefits of using SAR and LES to understand other atmospheric phenomena.

2 Methods

2.1 Observation data

On 2 October 2020, the Synthetic Aperture Radar (SAR) on board the Sentinel-1B satellite flew over the English Channel at 6:23 UTC capturing Storm Alex's surface signature in Interferometric Wide mode with swath width of 250 km (yellow shaded area in Fig. 1). The C-band SAR, emitting at 5.405 GHz, provides dual-polarised images, emitting in Vertical polarisation and then receiving in both Vertical (VV signal, referred to as co-pol) and Horizontal polarisation (VH signal, referred to as cross-pol) (Mouche et al., 2019). The backscattering from the VV and VH signal has a spatial resolution of 10×10 m. SAR backscatter, commonly expressed as the normalised radar cross section (σ_0), is highly sensitive to centimetre-scale capillary and short gravity waves through different scattering mechanisms in co- (Valenzuela, 1978; Kudryavtsev et al., 2005) and cross-polarisations (Valenzuela, 1967; Voronovich and Zavorotny, 2013). The slope distribution of these waves controls the sea surface roughness sensed by SAR and provides an indirect link between σ_0 and near-surface wind forcing, including friction velocity. With the co-polarised and cross-polarised signals ocean surface wind speed can be estimated with the algorithm presented in Mouche et al. (2019). The wind fields provided, although estimated from SAR images in IW mode, i.e., with spatial resolutions of 10 m in the Level-1 product, are downgraded to 1 km resolution in the Level-2 wind product, allowing a better comparison of SAR winds with the 1-minute averaged winds from observations. Another product at 200 m resolution is added in this study to provide fine scale wind values and sea surface roughness observations.

Data from ASCAT, a radar emitting at 5.255 GHz on MetOp-A and operating only in co-polarisation (VV), is also used in this study. ASCAT is able to reliably measure wind speeds, but starts to underestimate them above 25 $\mathrm{m\,s^{-1}}$ (Polverari et al., 2021). In fact, it loses sensitivity and the signal begins to significantly saturate as the C-band backscatter loses sensitivity in VV. The horizontal resolution (12.5 km) is coarser and its coverage is larger compared to SAR data, thus the data is used to characterise the mesoscale structure of Storm Alex and its trajectory during the day of 2 October, with two passes at 08:50 UTC and 11:00 UTC over the British Channel.

https://doi.org/10.5194/egusphere-2026-3679
Preprint. Discussion started: 20 July 2026
© Author(s) 2026. CC BY 4.0 License.

Cloud top temperatures associated to Storm Alex are estimated from brightness temperature measured by the 10.8 μm channel on the Spinning Enhanced Visible and InfraRed Imager (SEVIRI) radiometer on the Meteosat Second Generation (MSG) geostationary satellite. The horizontal resolution is 3 km for infrared imagery each 5 minutes. Data from the visible channel, with a finer resolution of 1 km, is not used due to the timing of the case study focusing around the SAR acquisition which occurred during the night to day transition.

Another valuable source of information regarding Storm Alex comes from ground-based remote sensing. Operational radar-derived quantitative precipitation estimates from the Météo-France Mosaic ARAMIS network are used, providing 5-minute rainfall accumulations at 1 km of horizontal resolution (Figueras i Ventura and Tabary, 2013). The Jersey radar site is used to complete the precipitation over the British Channel. MSG and radar data are used to validate the simulated location of the different fronts associated with Storm Alex.

In order to supplement remote sensing, this study uses in situ 10-m wind measurements averaged over 10 minutes. Fourteen coastal weather stations are included to ensure synergy with satellite observations and numerical simulations. Nine stations are operated by Météo-France and located in the French departments of Manche (7) and Côtes-d'Armor (2), and five other stations are operated by the UK Met Office and located in south-west England (3), Guernsey (1) and Jersey (1) (See Fig. 2 for location). In the British Channel, an anemometer positioned at 14 m above sea level on a buoy located at 49.9°N 2.9°W (named buoy 62103 maintained by the UK Met Office) and one on a ship (EUCFR03, Giraldo and Le Roy (2020)) are added to the in situ measurement. The measurement data collected at sea is very valuable, as it also allows wind products from satellites (i.e., ASCAT and SAR) to be validated close to the centre of Storm Alex. Lastly, a radiosounding at 5:00 UTC from the Larkhill station (UK) offers a vertical profile of wind speed to the north-east of the extratropical cyclone.

2.2 Configuration of numerical simulations

Numerical simulations are carried out using the non-hydrostatic atmospheric research model Meso-NH (Lac et al., 2018) in its version 5.5.1 ported on GPU (Graphics Processing Unit; Escobar et al. (2025)). This architecture enables faster production of LES with significant reductions in energy consumption. To investigate the mesoscale and fine-scale dynamics associated with Storm Alex, simulations with increasing horizontal resolution are performed as shown in Fig. 1.

The first simulation, called MNH800 (blue domain in Fig. 1) is initialised using IFS analyses (horizontal resolution ≈ 9 km) at 00:00 UTC on 2 October 2020. The 06:00 and 12:00 UTC IFS analyses are used as lateral boundary conditions for MNH800. The simulation covers a 12 h) period from 00 to 12 UTC, with a time step of 8 s) and output data stored every 10 minutes. The horizontal grid spacing of this simulation is of 800 m over a 512 × 512 grid points domain, corresponding to an area of approximately 410 × 410 km^2, covering the spatial extent from 5.5°W to 0.5°E of longitude and 48° to 52°N of latitude, thus encompassing the SAR swath (yellow area in Fig.1). The vertical discretisation consists of 92 levels, matching the configuration of the operational AROME model (Brousseau et al., 2016), with a stretching of resolution over the vertical grid from 5 m at the surface to more than 2 km in the stratosphere (27 km). A 4th order centered scheme is used for advection to achieve a high effective resolution while the turbulence scheme is one dimensional with a mixing length computed according to Bougeault and Lacarrere (1989). Deep convection is explicitly resolved whereas shallow convection is parametrised with

https://doi.org/10.5194/egusphere-2026-3679
Preprint. Discussion started: 20 July 2026
© Author(s) 2026. CC BY 4.0 License.

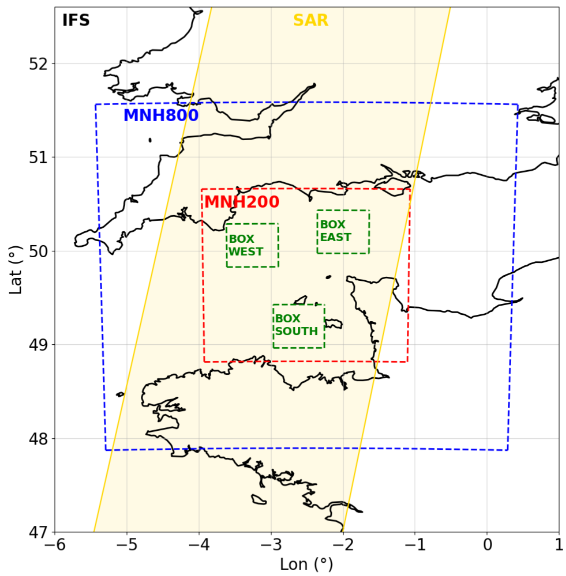

Figure 1. Map of domains for the MNH800 simulation (in blue), the MNH200 simulation (in red) and the three Large-Eddy Simulations (in green). The IFS domain covers all simulations and the yellow shaded area represents the SAR swath.

an eddy-diffusive mass-flux scheme (Pergaud et al., 2009). The ICE3 microphysics scheme is used to simulate mixed-phase cloud processes (Pinty and Jabouille, 1998). SURFEX (Masson et al., 2013) is used as surface scheme for fluxes and WASP (Wave-Age dependent Stress Parameterization, Bouin et al. (2024)) for ocean surface. Additionally, the radiative transfer model RTTOV (Saunders et al., 2018) version 13.2 is activated to enable satellite radiance simulations for observation-model comparisons (Chaboureau and Pinty, 2006), in particular the infrared brightness temperature (T_B) for channel 10.8 µm.

The second simulation, called MNH200 (red domain in Fig. 1), is a zoom within MNH800 with the same center. The domain extent is divided by 2 whereas the horizontal resolution is increased by 4 (Δx = 200 m, 1024 x 1024 grid points) and the time step adjusted proportionally (Δt = 2 s). The simulation lasts 3 hours, starting at 05:00 UTC and ending at 08:00 UTC. Initial and lateral boundary conditions are given by MNH800 each 10 minutes. MNH200 uses the same physical parameterisations as MNH800 except for a 3D turbulence scheme (Cuxart et al., 2000) with the Deardorff mixing length (Deardorff, 1980). In addition, the shallow convection scheme is deactivated.

In order to investigate the fine-scale structures and to match the horizontal resolution of SAR observations, three Large-Eddy Simulations (LESs) are performed with a horizontal grid spacing of 50 m, in a domain of approximately 50 × 50 km^2 (1024 x 1024 grid points each, green domains in Fig. 1) and a time step of 0.5 s. MNH200 serves as initial and lateral conditions for LESs each 10 minutes. Each LES is started at 05:30 UTC once fine-scale structures are formed in MNH200 and to allow a long enough spin-up before the target analysis time of 6:23 UTC. The LESs are run until 08:00 UTC. Also, between 70% and 80% of the Turbulent Kinetic Energy (TKE) is resolved at the surface (up to 90% within the boundary layer) across all three

https://doi.org/10.5194/egusphere-2026-3679
Preprint. Discussion started: 20 July 2026
© Author(s) 2026. CC BY 4.0 License.

LESs, indicating a consistent representation of the surface circulation. Hereafter, the three LESs are referred to as Box East, Box South and Box West (Fig. 1).

Due to the substantial computational cost of simulations, MNH200 and LES are run on the GPU partition of the ADASTRA supercomputer (Escobar et al., 2025), representing 7 computing hours with 2 GPU-nodes and 6 hours with 4 GPU-nodes, respectively.

2.3 Model diagnostics

Extratropical cyclones, such as Storm Alex, are characterised by contrasting air masses associated with distinct warm and cold sectors. The equivalent potential temperature θ_e is used to identify these air masses, and is computed as follows:

$$\theta_e = \theta \exp\left(\frac{L_v r_s}{c_p T}\right) \tag{1}$$

where θ denotes the potential temperature, L_v the latent heat of vaporisation, r_s the saturation mixing ratio, c_p the specific heat capacity of dry air, and T the absolute temperature.

Numerical variables such as 10-m wind speed, hereafter referred to as surface wind and denoted by U_{10}, and surface roughness length z_0 are used to compare simulation outputs and SAR. The U_{10} in Meso-NH is diagnosed using the Monin–Obukhov similarity theory (Monin and Obukhov, 1954). The main relationship is given by:

$$U(z) = \frac{u_*}{k}\left[\ln\left(\frac{z}{z_0}\right) - \psi_m\left(\frac{z}{L}\right)\right] \tag{2}$$

where u_* is the friction velocity, k is the von Kármán constant ($k \approx 0.4$), L is the Monin–Obukhov length, and ψ_m is the stability correction function for momentum. The roughness length (z_0) is defined with the externalised surface model SURFEX as the sum of rough and viscous regimes as:

$$z_0 = u_*^2 \frac{\alpha}{g} + 0.11\frac{\nu}{u_*} \quad \text{and} \quad u_* = U_{10}\sqrt{C_d} \tag{3}$$

where α and ν correspond to the Charnock coefficient and the kinematic viscosity of dry air, respectively, and C_d the drag coefficient.

The SURFEX parametrisation used in this study is WASP (Bouin et al., 2024). The Charnock coefficient is dependent on the age of the wind-sea, which is particularly useful for areas of high wind speeds over the sea. An initial estimate for calculating U_{10} is obtained by setting the Charnock constant, C_d, and z_0 using Eq. 2. From U_{10}, a value for u_* is derived, followed by z_0 with Eq. 3, which is then fed back into the Monin–Obukhov relationship (Eq. 2). For low winds (< 1 $\mathrm{m\,s^{-1}}$), a single iteration is sufficient; otherwise, three iterations are required. Typical range for z_0 on sea is between 10^{-5} and $10^{-3}\ \mathrm{m^{-1}}$ for U_{10} lower than 10 $\mathrm{m\,s^{-1}}$ and 10^{-3} to $10^{-2}\ \mathrm{m^{-1}}$ for U_{10} higher than 30 $\mathrm{m\,s^{-1}}$. It is assumed that the roughness length z_0 obtained from simulations exhibits a similar dependence on surface wind as the backscattering σ_0 obtained from SAR measurements, since both are related to the friction velocity u_*. However, this assumption should be treated with caution, as z_0 and σ_0 are sensitive

https://doi.org/10.5194/egusphere-2026-3679
Preprint. Discussion started: 20 July 2026
© Author(s) 2026. CC BY 4.0 License.

to different scales of surface roughness (e.g. these scales changes with respect to the radar frequency, the polarization and the incidence angle).

The Marine Atmospheric Boundary Layer (MABL) height is defined as the altitude where the Richardson number (Ri) first exceeds 0.25. Ri is diagnosed using the gradient Richardson number method:

$$Ri = \frac{g}{\rho} \frac{\frac{\partial \rho}{\partial z}}{\left(\frac{\partial u}{\partial z}\right)^2} \tag{4}$$

where ρ is the air density, u the horizontal wind speed, and $\partial/\partial z$ represents the vertical derivative of a variable. It provides a physically based estimate of the transition between the turbulent boundary layer and the free atmosphere by accounting for both thermal stratification and wind shear. This approach is particularly suitable under strongly windy conditions associated with Storm Alex. A negative Ri indicates thermally unstable conditions (i.e., convective mixing), whereas $Ri > 0.25$ corresponds to a stable regime. Between these two limits ($0 < Ri < 0.25$), turbulence may persist under weakly stratified or near-neutral conditions.

2.4 2-D Autocorrelation function

As 1D signal processing, significant effort has been invested in determining two-dimensional atmospheric pattern (Lohou et al., 1998; Mourad et al., 2000). Here, we propose using an autocorrelation function (ACF) developed by Granero Belinchon et al. (2022) and previously applied to SAR images (Brilouet et al., 2023) as well as LES outputs (Lfarh et al., 2023).

The first step in ACF analysis is to determine how the signal correlates with its neighbours in both x and y directions. The result shows whether a signal repeats and determines its shape. The second step is to determine whether patterns have a preferred orientation. In the spectral space, the directional dependence of the autocorrelation is assessed at the centre of the domain (Lohou et al., 1998). When the signal is anisotropic, an elliptical shape emerges around this point; otherwise, the pattern is circular. The major axis of the ellipse defines the preferential orientation of the autocorrelation pattern. The degree of elongation of the ellipse is quantified by the flatness parameter f (major minus minor axis divided by major axis). Values of f approaching 1 indicate that the autocorrelation structures are nearly linear, whereas values tending toward 0 correspond to a nearly circular shape. The third step is to determine the lengthscale of the organised structure (noted L_{os}). L_{os} can be determined only if f> 0.7 (Brilouet et al., 2023)) and corresponds to the distance between two maxima of autocorrelation in the direction perpendicular to the preferred orientation of organised structures.

3 Mesoscale structure and model evaluation

3.1 Synthetic Aperture Radar observations

The mesoscale structure of Storm Alex is well observed by SAR and fits within the satellite's swath as shown in Figure 2a. A low backscattering signal (dark) is located on the west of the Cotentin Peninsula (2-3°W; 49.3-50°N) and is surrounded by a

https://doi.org/10.5194/egusphere-2026-3679
Preprint. Discussion started: 20 July 2026
© Author(s) 2026. CC BY 4.0 License.

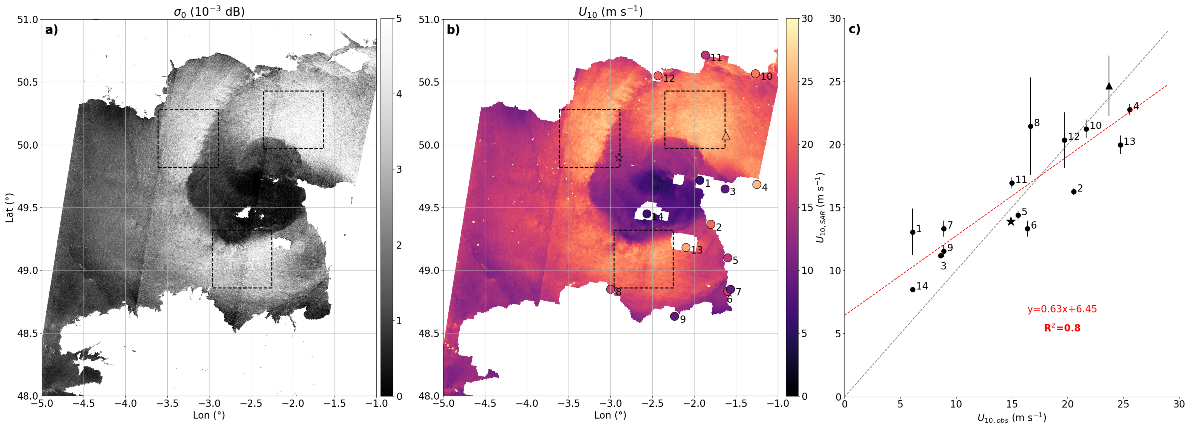

Figure 2. Map of a) Sea surface roughness from cross-polarisation backscattering signal σ_0 and b) horizontal surface wind speed U_{10} from Synthetic Aperture Radar observations on 2 October 2020 at 6:23 UTC. Observations from weather stations, buoy and ship are represented by green points, star and triangle, respectively, where inside color represents the measured surface wind. Dotted squares represent the LES domains. c) Comparison of observed surface wind speed by weather stations, buoy and ship ($U_{10,obs}$) and SAR estimation ($U_{10,SAR}$). The black and red dotted lines represent the linear regression and the perfect correlation, respectively

wrapping region of strong backscattering (bright) reaching the northern and southern borders of the Channel. Also, one of the main findings is the presence of a very pronounced front around the centre, corresponding to an abrupt transition from low to high backscatter. As expected, low wind speed (below 10 $\mathrm{m\,s^{-1}}$) is located in the same area of low backscattering signal while surface wind estimated by SAR exceeds 20 $\mathrm{m\,s^{-1}}$ in the wrapping region (Fig. 2b). Further west (longitude < 3.5°W), the wind remains moderate at around 10 to 15 $\mathrm{m\,s^{-1}}$. A thin band of light wind, associated to a front with weaker backscattering signal, is located in the north-western part of Storm Alex (3°W; 50-50.5°N). Three areas of strong surface winds are visible, where the surface wind speed locally reaches 30 $\mathrm{m\,s^{-1}}$: in the north-east (2.5° to 1.5° W and 50° to 50.5°N), north-west (3.5° to 3°W and 49.8° to 50.5°N) and south of Storm Alex (3° to 2° W and 48.7° to 49.3°N). The three high-resolution simulations (LES; horizontal grid spacing of 50 m) are centered on these three areas with high wind speed (dotted squares in Fig. 2a, b).

The SAR wind estimate was previously calibrated on other weather phenomena such as hurricanes (Mouche et al., 2017), where wind speeds are significantly higher than those observed in an extratropical cyclone. To ensure the reliability of the SAR wind estimates in the case of Storm Alex, they are validated against wind speed measurements from French meteorological stations at 06:24 UTC and from English stations at 06:30 UTC (see points in Fig. 2b). As SAR wind products are only available over the sea, direct co-location with weather stations is not possible and SAR wind values are averaged within a 2 km radius around each station. The floating buoy and ship also allow wind measurements in the open ocean (green star and triangle in Fig.2). For surface wind speeds below 10 $\mathrm{m\,s^{-1}}$, the SAR wind speeds are higher than station observations by 3-5 $\mathrm{m\,s^{-1}}$ (Fig. 2c). In addition, because the stations are located along the coast, wind speeds are likely reduced when the airflow originates from land toward the sea, which may explain the observed differences (e.g., stations 1 and 9 for example). For winds above

https://doi.org/10.5194/egusphere-2026-3679
Preprint. Discussion started: 20 July 2026
© Author(s) 2026. CC BY 4.0 License.

15 $\mathrm{m\,s^{-1}}$, SAR winds better match with the observed values with a slight underestimation of 0.5 $\mathrm{m\,s^{-1}}$. The linear regression between SAR and in situ winds has a slope of 0.63 and R^2=0.8. However, SAR estimations are consistent with observational data at sea, i.e. buoy and ship (star and triangle in Fig. 2) with a deviation less than 0.7 $\mathrm{m\,s^{-1}}$ SAR data therefore provides a good benchmark for comparing areas of strong winds (> 15 $\mathrm{m\,s^{-1}}$) derived from simulations at sea.

3.2 Validation of Alex' mesoscale structure

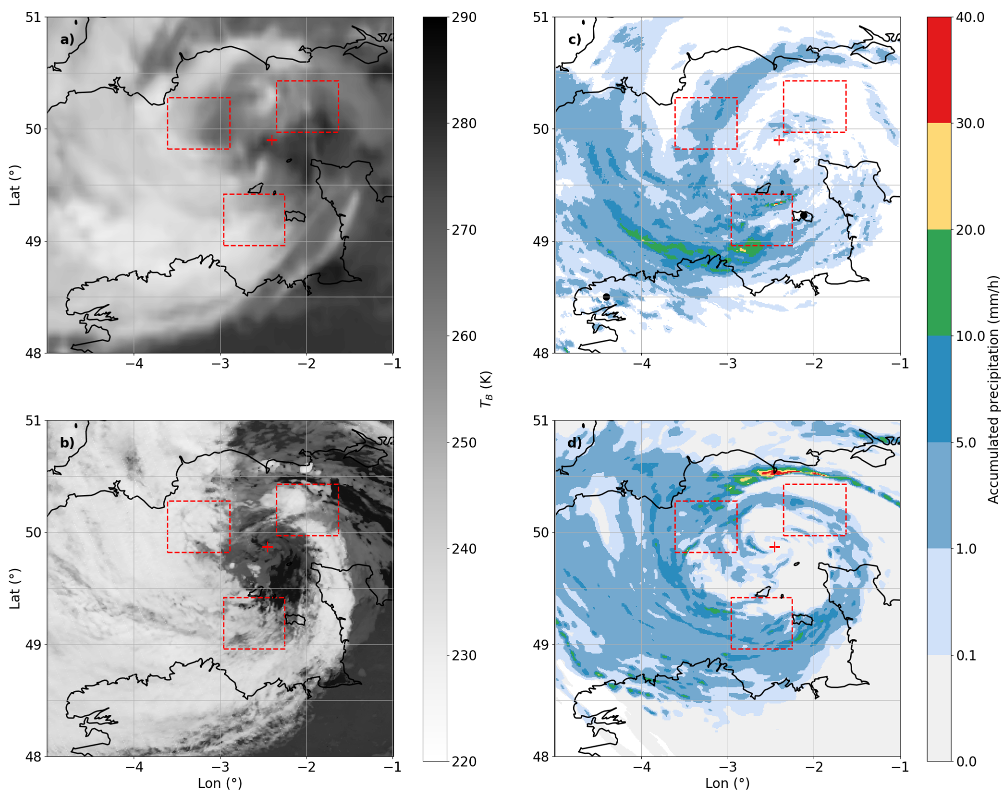

Figure 3. Map of brightness temperature from a) MSG and b) MNH800 at 6:30 UTC and accumulated precipitation between 6:25 and 6:30 UTC expressed in $\mathrm{mm\,h^{-1}}$ from c) radar and d) MNH800. Red squares represent the three LES domains, red crosses the centre of Storm Alex and black points in c) precipitation radar used in observations

This part is dedicated to assess the representation of the mesoscale structure of Storm Alex with MNH800. The synthetic observation of brightness temperature from MNH800 using RTTOV (Fig. 3c) is first compared to the MSG image (Fig. 3a) at 6:30 UTC. The centre of Storm Alex, defined as the location where the spiral ends with clear sky, is located around 2.2°W,

https://doi.org/10.5194/egusphere-2026-3679
Preprint. Discussion started: 20 July 2026
© Author(s) 2026. CC BY 4.0 License.

49.9°N (red cross in Fig. 3a,b) with MSG. The simulated center, defined as the location of the minimum mean sea level pressure (MSLP; 966 hPa), is well located at 2.4°W, 49.8°N (red cross in Fig. 3c,d). In the western part of Storm Alex, a wide cloudy area with brightness temperature (T_B) close to 240 K is observed, well simulated by MNH800. In the eastern part, a dry air intrusion coming from the south and that penetrates until 51°N is observed, whereas it is modelled by MNH800 but ends further south.

Precipitation data is combined with satellite observations and cloud structure data in order to locate fronts. High-frequency radar products allow for detailed examination of precipitation structures and intensities. Figure 3c shows two bands of precipitation. The first is located in the northern part of Storm Alex, characterised by a thin band of rain along the British coast with values between 5 and 10 $\mathrm{mm\,h^{-1}}$. It is co-located with the front of σ_0 (Fig. 2). The second is wider and more intense and located to the south-west of Storm Alex with precipitation between 10 and 20 $\mathrm{mm\,h^{-1}}$. The location of the two rain bands is well simulated by MNH800 while their intensity is different (Fig. 3d). The northern band has precipitation exceeding 30 $\mathrm{mm\,h^{-1}}$ while the southern band is defined by low precipitation between 1 and 10 $\mathrm{mm\,h^{-1}}$.

In summary, the simulated precipitation in Box South is lower than observed and a simulated clear sky area does not feature in the observations. In Box West, intense rain is simulated at the northern border while radar values indicates lower precipitation. This discrepancy can be due to the large distance between the precipitation area and the radar site (black dot in Fig. 3), which may affect the representativeness of the radar measurements (Champeaux et al., 2011). Finally, Box East shows low simulated precipitation as observed, although the precipitation rate is slightly higher towards the centre of the Box (maximum of 6 $\mathrm{mm\,h^{-1}}$ compared with the observed 3 $\mathrm{mm\,h^{-1}}$).

3.3 Mesoscale wind validation

The radiosounding at 5:00 UTC (black curve in Fig. 4a) shows a ground surface wind equal to 12 $\mathrm{m\,s^{-1}}$, then increases to around 28 $\mathrm{m\,s^{-1}}$ at 800 m, which indicates a LLJ associated with Storm Alex. The wind speed then decreases, stabilising at around 20 $\mathrm{m\,s^{-1}}$ above 4 km altitude. The simulated wind speed from MNH800 (blue curve in Fig. 4a) is slightly overestimated between 130 m (ground level) and 400 m. The maximum intensity of the LLJ is underestimated by approximately 3 $\mathrm{m\,s^{-1}}$ although its altitude, approximately 730 m, is correct.

In order to assess whether the MNH800 simulation represents surface wind adequately, comparisons are made with satellite retrievals. At 6:23 UTC, MNH800 wind speeds (Fig. 4c) are compared to SAR wind products (Fig. 4b). The simulation captures the three high wind speed areas localised around the low level pressure. The front located to the north of Storm Alex is well localised even if it is more curved than observed. Simulated surface winds in the three areas are systematically underestimated by about 3 $\mathrm{m\,s^{-1}}$, while in the entire simulating domain the simulated mean wind speed is very close to observations (Fig. 4d). Probability density functions (PDF) of surface winds show that strong wind extremes do not exceed 25 $\mathrm{m\,s^{-1}}$ in MNH800, whereas they reach 30 $\mathrm{m\,s^{-1}}$ in SAR winds.

At 8:50 UTC, Storm Alex has moved south-westward (Fig. 4e) with weaker winds from ASCAT compared to the SAR measurements recorded two and a half hours earlier (maximum wind speed around 21 $\mathrm{m\,s^{-1}}$). In MNH800 (Fig. 4f), the centre of the cyclone associated with weak winds and the surrounding areas of strong winds are well positioned. The situation is

https://doi.org/10.5194/egusphere-2026-3679
Preprint. Discussion started: 20 July 2026
© Author(s) 2026. CC BY 4.0 License.

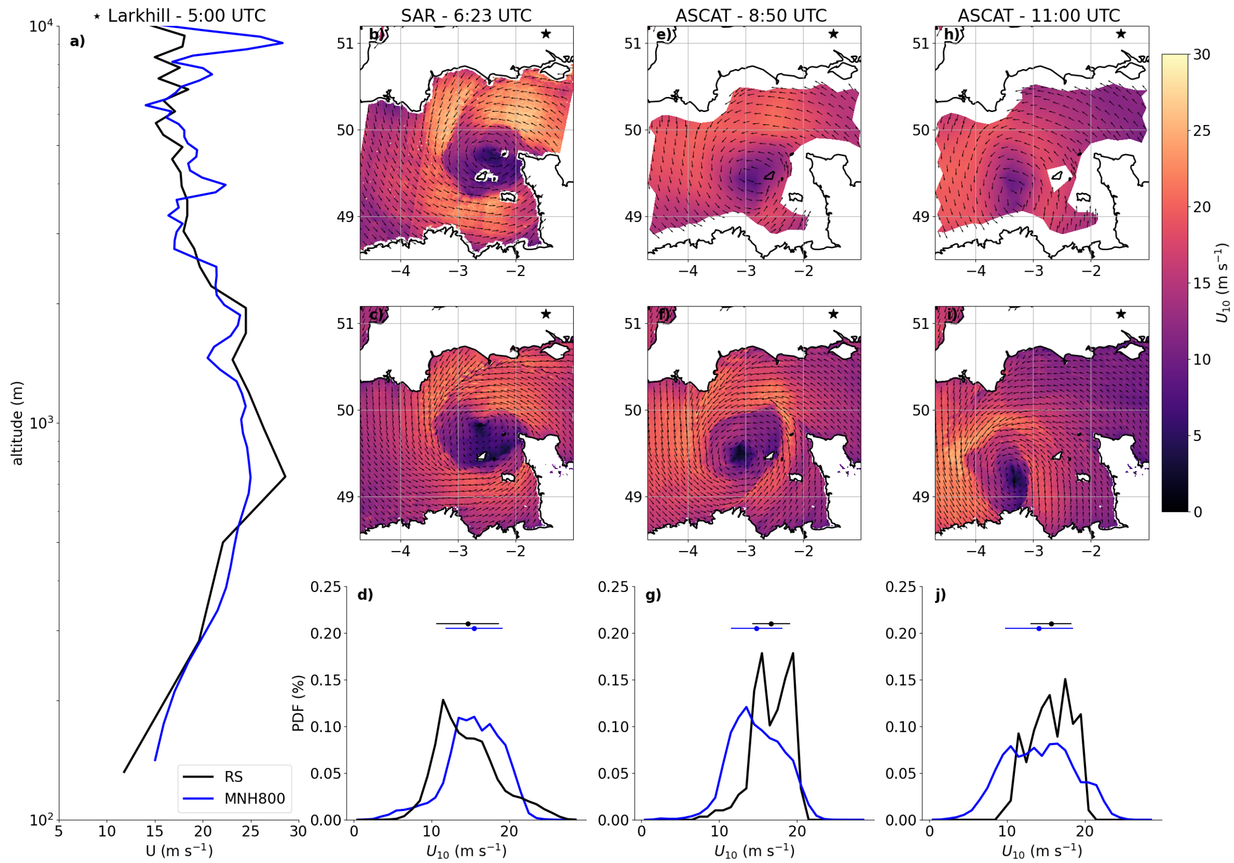

Figure 4. a) Vertical profile of horizontal wind speed at the Larkhill station for the radiosounding (in black) and MNH800 (in blue). Maps of surface wind speed at 6:23 UTC for b) SAR observations and c) MNH800, at 8:50 UTC for e) ASCAT observations and f) MNH800 and at 11:00 UTC for h) ASCAT observations and i) MNH800. The black star represents the Larkhill station location. Probability density functions of surface wind speed for d) SAR, g) and j) ASCAT (black) and MNH800 (blue).

similar at 11:00 UTC during the second ASCAT pass, when the cyclone centre has moved further towards the south-west (Fig. 4h,i). The mean observed winds are underestimated by MNH800 (14.8 $\mathrm{m\,s^{-1}}$ versus 16.2 $\mathrm{m\,s^{-1}}$ at 8:50 UTC, Fig.4g; 14.2 $\mathrm{m\,s^{-1}}$ versus 16 $\mathrm{m\,s^{-1}}$ at 11:00 UTC, Fig.4j). By degrading the horizontal resolution of the MNH800 simulation output to match with the ASCAT resolution (i.e., 12.5 km) and removing coastal pixels, the mean surface wind from MNH800 increases by 0.5 $\mathrm{m\,s^{-1}}$ at 8:50 UTC and 0.6 $\mathrm{m\,s^{-1}}$ at 11:00 UTC and the MNH800 distribution is closer to ASCAT (not shown). This can be partly explained by the exclusion of the coastal zone, where surface wind speeds are low. Comparing the distributions (Fig. 4g,j), the simulated surface wind extremes (low or high) are greater than those observed, with a flatter distribution. This may be the result of the finer resolution in the simulation and this widening is reduced when the resolution is degraded (not shown).

https://doi.org/10.5194/egusphere-2026-3679
Preprint. Discussion started: 20 July 2026
© Author(s) 2026. CC BY 4.0 License.

Given the underestimation of winds relative to the SAR, various sensitivity tests were performed but are not shown here for the sake of conciseness. Using high-resolution analyses for initial and boundary conditions from the Arome operational model (Seity et al., 2011) instead of IFS produced a slight increase in wind speed but does not solve the general underestimation in all three Boxes. This suggests an underestimation of wind speed in the initial conditions given by the parent models. Similarly, using the COARE 3.0 (Fairall et al., 1996) and ECUME (Belamari, 2005) parameterisations of surface turbulent fluxes over the sea instead of WASP only shows a slight decrease (-0.2 $\mathrm{m\,s^{-1}}$) or increase (+0.3 $\mathrm{m\,s^{-1}}$) in wind speed, respectively. This low sensitivity is due to the surface wind range, which is not suitable for wind improvement with surface models (Bouin et al., 2024). One other possible explanation for wind underestimation could also come from the atmosphere's response to sea surface temperature (SST). Bador et al. (2025) shows that a 2 K increase in SST has the effect of increasing the wind gusts of Storm Alex over the English Channel by around 4 to 8 $\mathrm{m\,s^{-1}}$, due to the cyclone becoming more intense. Indeed, two available SST observations show that the model SST is slightly underestimated by 0.4 to 0.5 K in the MNH800 simulation (buoy, star in Fig.2b: 289.34 K versus 288.86 K; ship, triangle in Fig.2b: 290.25 K versus 289.82 K).

In conclusion, MNH800 successfully localises the three high-wind areas corresponding to the three Boxes. However, a surface wind underestimation of approximately 1 $\mathrm{m\,s^{-1}}$ is found in the whole domain compared to satellite observations and is stronger in the three Boxes (3–4 $\mathrm{m\,s^{-1}}$).

3.4 Airmass identification relative to high wind speed regions

Figure 5 shows fields characterising the thermodynamics of Storm Alex at 6:23 UTC from the MNH800 simulation, where the three areas of strong winds are shown by black dotted Boxes. The equivalent potential temperature θ_e at 500 m (see Eq. 1) in Fig. 5a shows a warm area (warm seclusion) trapped in the centre of the cyclone (θ_e > 14 °C). It is surrounded by cold air that penetrates from the south, along with the dry air intrusion (Fig. 3c). The interface is characterised by a warm front, which is associated with a sharp decrease in surface wind speed and the heaviest precipitation. The MABL height (Fig. 5b) reaches less than 200 m in the centre of the cyclone and is more variable in windy areas, ranging from 200 to over 1000 m. In Box East, the MABL height increase from 400 m in cold air to more than 800 m close to the warm front. In Box South, the MABL height is slightly lower between 300 to 500 m, while it varies the most in Box West with peaks of up to 830 m. It is generally higher when θ_e is higher.

Strong surface winds in Boxes East and South (Fig. 4b) are occurring in the CCB (θ_e<13 °C) ahead of the warm front. Box West, meanwhile, is located directly on the front, which is less pronounced than in the other two Boxes. The maximum wind speeds from the surface up to 4 km (Fig.5c) are also located ahead of the warm front, in the CCB. Maximum winds are stronger in Box West (> 35 $\mathrm{m\,s^{-1}}$) than in Boxes South and East (25 to 35 $\mathrm{m\,s^{-1}}$). The altitude of maximum wind speeds also varies spatially (Fig.5d). In Boxes East and South, peaks of LLJ are found between 400 and 800 m, whereas in Box West they occur at higher levels, between 600 and 1500 m, indicating a deeper vertical extent of the LLJ in this region (in agreement with Fig.4a).

https://doi.org/10.5194/egusphere-2026-3679
Preprint. Discussion started: 20 July 2026
© Author(s) 2026. CC BY 4.0 License.

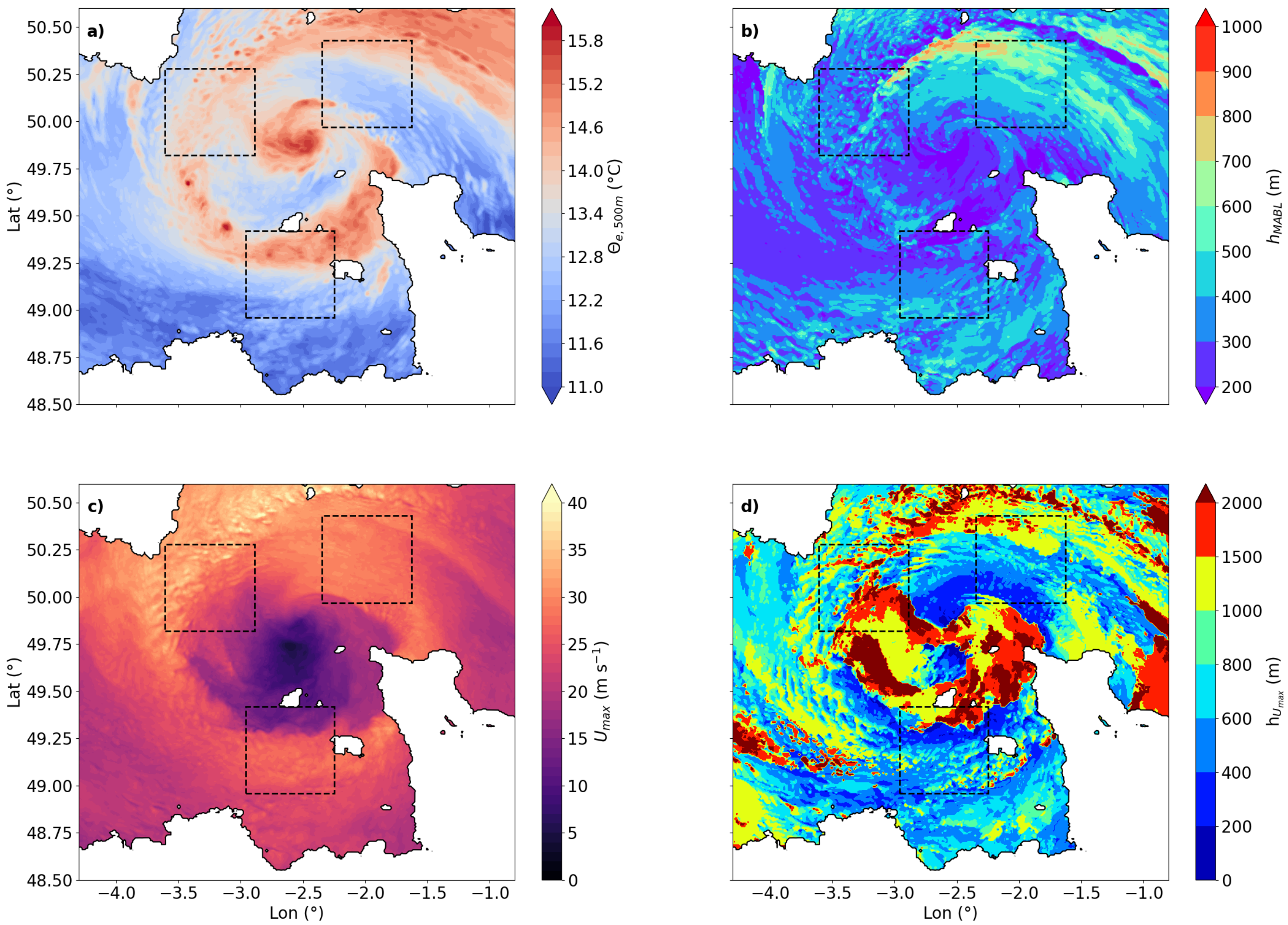

Figure 5. Map of the a) equivalent potential temperature θ_e at 500 m, b) marine boundary layer height, c) maximum horizontal wind speed up to 3 km altitude and d) its corresponding altitude, from the 6:23 UTC output of MNH800. The dotted black Boxes indicate the three LES domains.

The three Boxes exhibit surface winds of comparable intensity, yet they are located in thermodynamically distinct regions. To better understand how these differences influence surface wind, the role of fine-scale processes is investigated in the following section using LES.

4 Fine-scale processes at play in the windstorm

Since the MNH800 simulation correctly represents the strong surface winds associated with Storm Alex, it is used to provide three LESs: one in each identified region of interest (see black Boxes in Fig. 5) which have distinct environmental conditions. The LESs are analysed to investigate the mechanisms responsible for surface wind generation. First the surface winds in the

https://doi.org/10.5194/egusphere-2026-3679
Preprint. Discussion started: 20 July 2026
© Author(s) 2026. CC BY 4.0 License.

LES are evaluated in order to assess their ability to adequately capture fine scale surface organisation. The surface organisation is then qualified based on both the SAR backscatter data and the LES surface roughness. It is then linked to vertical MABL coherent structures. Finally, factors influencing MABL organisation are put forward.

4.1 Surface wind

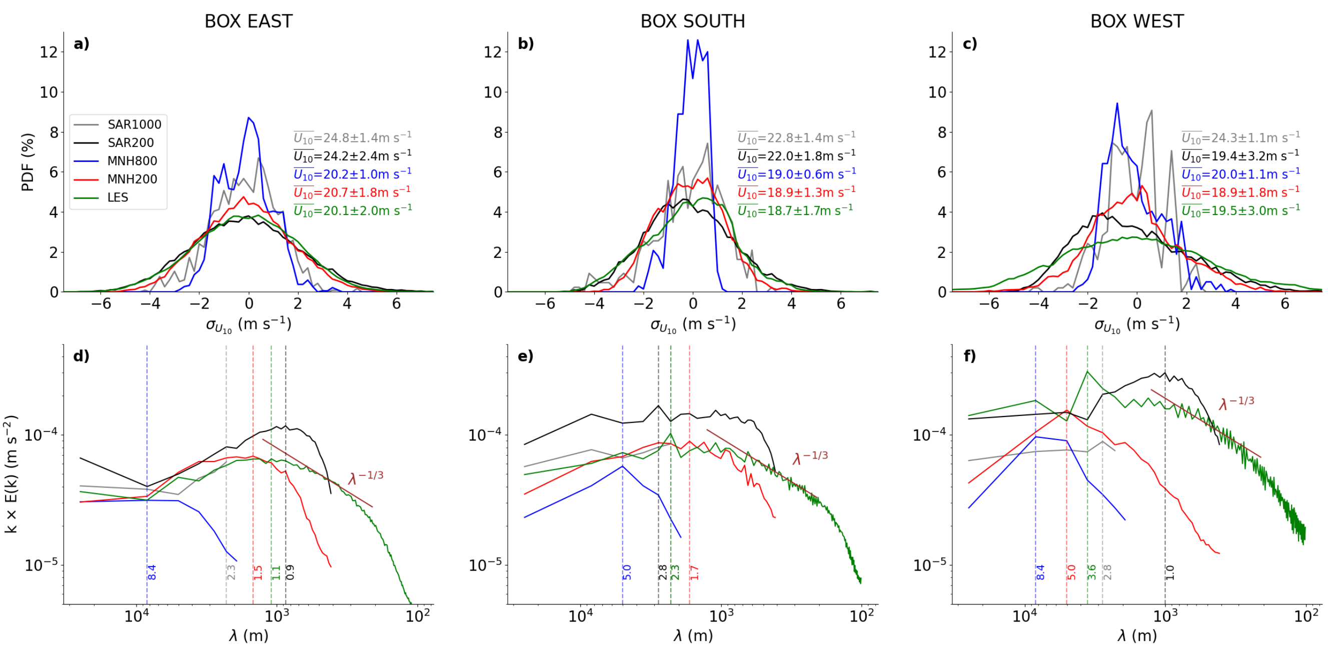

Figure 6. Probability density functions of surface wind speed deviations from the mean for Boxes (a) East, (b) South, and (c) West, together with the corresponding energy spectra in panels (d), (e), and (f). Estimates from SAR are shown at 1 km resolution (grey line) and 200 m resolution (black line). Simulations from MNH800, MNH200, and LES are represented by the blue, red, and green lines, respectively. Vertical dotted lines indicate the wavelengths of maximum energy and brown lines correspond to the spectral slope of the Kolmogorov cascade.

The ability of the LESs to reproduce the diversity of surface winds within the three Storm Alex Boxes is assessed against SAR-derived surface wind products at horizontal resolutions of 1 km and 200 m. Compared with SAR products, all simulations, irrespective of domain configuration or horizontal resolution, systematically underestimate the mean surface wind speed by ∼4 $\mathrm{m\,s^{-1}}$. Increasing the resolution does not compensate for this bias, suggesting that other factors are responsible, as discussed in Section 3.3. Wind speed anomalies relative to the domain-mean value are then compared in each box (Fig. 6a–c). Across the three Boxes, the mean surface wind speed even exhibits a slight decrease as horizontal grid spacing is refined from 800 m to 50 m. The reduction amounts to -0.1 $\mathrm{m\,s^{-1}}$ in Box East (panel a), -0.4 $\mathrm{m\,s^{-1}}$ in Box South (panel b), and -0.5 $\mathrm{m\,s^{-1}}$ in Box West (panel c). In the last case, part of the decrease may also result from the westward displacement of the frontal system in LES.

https://doi.org/10.5194/egusphere-2026-3679
Preprint. Discussion started: 20 July 2026
© Author(s) 2026. CC BY 4.0 License.

For Boxes East and South (panels a–b), the probability density functions (PDFs) of SAR and LES winds are approximately Gaussian, whereas Box West (panel c) exhibits noisier and more asymmetric distributions. As model resolution increases, the PDFs become progressively flatter, indicating enhanced variability. The standard deviation increases by approximately +1 $\mathrm{m\,s^{-1}}$ in Boxes East and South and by +1.4 $\mathrm{m\,s^{-1}}$ in Box West. Similarly, the high resolution SAR200 wind product displays broader PDFs than SAR1000. Consequently, simulated extreme wind values at 200 m and 50 m resolutions are in closer agreement with SAR observations. LES outputs degraded to the MNH800 resolution remain more spread than the original MNH800 simulation (not shown), indicating that part of the variability arises from explicitly resolved fine-scale dynamics rather than from increases in the number of grid points alone.

To evaluate whether a 50 m horizontal resolution is sufficient to represent MABL circulations and their associated energy content, kinetic energy spectra are analysed in both simulations and observations (Fig. 6d–f). The SAR1000 spectra (grey curves in Fig. 6d–f) are computed in two dimensions, whereas those derived from SAR200 (black curves) are only calculated along the cross-wind direction owing to strong speckle contamination. The SAR1000 spectra show an increase in energy for wavelengths below 5 km. However, the spectral analysis are limited by the spatial resolution (i.e., 1 km) and are truncated at approximately 2 km. Therefore, the energy increase toward finer scales cannot be assessed from SAR1000 data. Energy spectra derived from SAR200 exhibit enhanced energy at kilometre scales, with peak near λ=0.9 km in Box East (Fig. 6d) and λ=1 km in Box West (Fig. 6f). In contrast, energy remains relatively constant across kilometre scales in Box South (Fig. 6e). The sharp decrease in energy below λ=800 m observed in all three Boxes reflects the effective resolution limit of the SAR wind products.

For MNH800 (blue curves in Fig. 6d–f), energy spectra decrease rapidly at fine scales, which indicate an effective resolution around 4–5 km and therefore insufficient to resolve boundary layer circulations. MNH200 simulations show contrasting behaviours among the three Boxes. In Box East (red curves in Fig. 6d), an accumulation of energy is evident, with a peak around λ=1.5 km. In Box South (Fig. 6e), the spectral shape resembles that of SAR200, with nearly constant energy at kilometre scales. In Box West (Fig. 6f), maximum energy occurs near λ=5 km before decreasing toward smaller scales, differing substantially from the SAR200 spectrum.

LES spectra are broadly consistent with SAR200 observations in Boxes East and South. In Box East (green curves in Fig. 6d), LES confirms the presence of enhanced energy at kilometre scales, with a peak shifted toward λ=1.1 km, closer to SAR observations. Below this peak, the spectral slope approaches the Kolmogorov scaling, indicating that LES explicitly resolves fine-scale surface-flow structures down to its effective resolution ($\sim$ 300 m), corresponding to approximately six times the grid spacing). In Box South (Fig. 6e), LES spectra display a slight increase in energy between λ=1 and 3 km, followed by an inertial-range behaviour characterised by $k \times E(k)$ scaling close to $k^{-2/3}$. This behaviour is consistent with Kolmogorov theory and suggests active turbulent energy transfer across scales down to λ=200 m (approximately four times the grid spacing). The main discrepancy between SAR and LES spectra occurs in Box West, where energy decreases continuously from large to fine scales without exhibiting the kilometre-scale energy peak identified in SAR observations. Overall, these results indicate that a 50 m horizontal resolution is sufficient to capture both the characteristic energy enhancement at kilometre scales and

https://doi.org/10.5194/egusphere-2026-3679
Preprint. Discussion started: 20 July 2026
© Author(s) 2026. CC BY 4.0 License.

the fine-scale organisation of the MABL. LES simulations reproduce several key spectral characteristics observed in SAR200 products for Boxes East and South, whereas notable differences remain in Box West.

These findings further suggest that fine-scale dynamical processes play an important role in high-wind regions and that increasing horizontal resolution enables their explicit representation. This leads to broader and more realistic surface wind distributions, in improved agreement with SAR observations. The physical mechanisms underlying these processes, as well as the remaining differences between SAR and LES, are examined in the following section.

4.2 Highlight of surface organised pattern in SAR and LES

The three Boxes are characterised by strong backscattering in SAR, around 5×10^{-3} dB (Fig.7a,c,e), i.e., a strong sea surface roughness caused by the wind (see Section 3.1). Linear structures alternating between areas of low backscattering (dark) and high backscattering (light), quasi-periodic and aligned with the surface wind can be identified as streaks (Wang et al., 2019, 2025). In addition, there are less linear surface patterns of several tens of kilometres in size at the interface between weak and strong backscattering and perpendicular to the wind. They can be attributed to mesoscale frontal instabilities (Harvey et al., 2017). To understand which fine-scale phenomena are responsible for the energy accumulation on the km-scale and objectively quantify the shape and size of the structures, an ACF (defined in section 2.4) is applied on σ_0 in SAR data on the one hand and roughness length z_0 (see Eq. 3) in LES on the other hand (Fig. 7).

Due to heterogeneity in the three Boxes (curved direction of streaks around Storm Alex center, contrasting areas of high and low backscattering in Boxes South and West), each Box is divided into subdomains measuring 5 by 5 km^2 (red squares in Fig. 7) following approaches in Zhang et al. (2008); Granero Belinchon et al. (2022). In each Box, a maximum of 100 subdomains can be analysed but several filters are applied beforehand. First, subdomains in SAR and LES with a mean surface wind speed below 20 $\mathrm{m\,s^{-1}}$ are removed (blue dots in Fig.7). The number of subdomains excluded for each Box is given in Table 1 as N_w. Second, the sides of the LES domains with inflow from lateral boundary conditions from the MNH200 model do not form the fine-scale structures expected with a resolution of 50 m. They are therefore removed (orange dots in south and east sides in Fig.7b, west side in Fig.7d, north and east sides in Fig.7f) and identified as N_p in Table 1. Third, in SAR images, some subdomains are excluded due to the presence of ships and/or submerged land, which interfere with the SAR signal (green dots in Fig.7a,c,e). They are also identified as N_p in Table 1. The total number of subdomains retained for the ACF analysis (N_v) is reported in Table 1. For Box East, 48 subdomains are retained from the LES dataset, compared with 89 from the SAR dataset. This number decreases for Box South, with 25 subdomains from LES and 31 from SAR, and for Box West, with 26 from LES and 69 from SAR. The discrepancy between LES and SAR mainly results from the suppression of LES subdomains influenced by lateral boundaries. In Box West, the reduced extent of the strong wind field further contributes to the strong decrease in the number of retained subdomains.

The ACF is applied to each subdomain and describes how the signal is organised in both horizontal directions. One subdomain in each Box for SAR and LES data is shown in Fig. 8 to illustrate the typical patterns found in Boxes. The results of the ACF are shown in the second and fourth columns. Positive values indicate that the signal is correlated with the point [0,0],

https://doi.org/10.5194/egusphere-2026-3679
Preprint. Discussion started: 20 July 2026
© Author(s) 2026. CC BY 4.0 License.

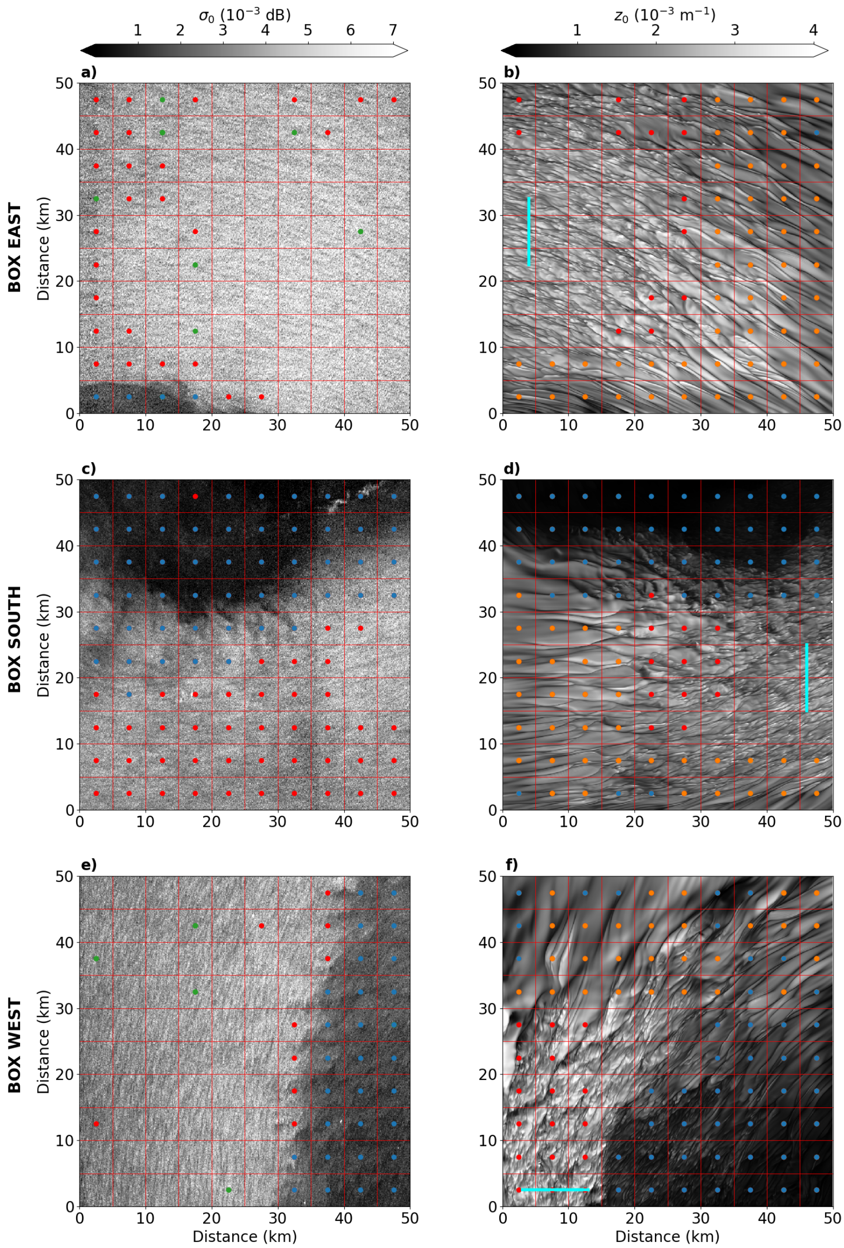

Figure 7. Backscattering σ_0 from SAR (10^{-3} dB, first column) and z_0 from LES ((10^{-3} m^{-1}, second column) for Boxes East (first line), South (second line) and West (third line). Red squares correspond to 5 x 5 km^2 subdomains and cyan lines correspond to the trace of vertical cross sections in LES. Blue dots indicate subdomains with surface wind speed < 20 $\mathrm{m\,s^{-1}}$; orange dots, subdomains undergoing advection; green dots, polluted subdomains; and red dots, subdomains with $f < 0.7$.

https://doi.org/10.5194/egusphere-2026-3679
Preprint. Discussion started: 20 July 2026
© Author(s) 2026. CC BY 4.0 License.

Box	variable	N_w	N_p	N_v	N_s	f	L_{os} (km)	$\Delta\Theta(°)$
EAST	z_0	0	52	48	35	0.83 ± 0.04	1.1 ± 0.5	24 ± 5
	σ_0	4	7	89	63	0.75 ± 0.08	1.2 ± 0.9	20 ± 16
SOUTH	z_0	23	52	25	13	0.83 ± 0.05	0.9 ± 0.5	13 ± 4
	σ_0	52	0	43	5	0.75 ± 0.03	1.1 ± 0.3	11 ± 23
WEST	z_0	22	52	26	9	0.8 ± 0.05	1.5± 0.8	-15 ± 11
	σ_0	27	4	69	59	0.83± 0.06	1.2± 0.8	-10 ± 11

Table 1. Summary of ACF metrics for Boxes East, South, and North. σ_0 is derived from SAR and z_0 from LES. N_w, N_p, N_v, and N_s denote, respectively, the number of subdomains with mean surface wind speed < 20 $\mathrm{m\,s^{-1}}$, polluted conditions, valid ACF, and identified streak structures (with $f > 0.7$ for Meso-NH). $\overline{L_{os}}$, $\overline{\Theta}$, and $\overline{\Delta\Theta}$ represent the mean flatness, the characteristic length scale of the structures (km), and the mean angular deviation between the structure orientation and the wind direction, respectively, computed over N_s subdomains.

while negative values indicate an anticorrelation. The direction of the maximum autocorrelation is represented by black dashed lines. The first local maximum of the autocorrelation is calculated perpendicular to this direction (blue stars).

According to Brilouet et al. (2023), f>0.7 in SAR data corresponds to streaks, while f<0.7 can be interpreted as a transition between cells and streaks. The N_s column in Table 1 reports the number of subdomains considered as streaks based on this criterion. Subdomains without streaks are represented by the red dots in Figure 7. In Box East streaks are present in 73% of the valid subdomains in LES, which is consistent with the SAR observations (71%). Contrasted results are found in the other two Boxes. While half of the valid subdomains in Box South are characterised by streaks in LES (52%), the SAR counts only 12%. In Box West, subdomains composed of streaks are a minority (36%), whereas in the SAR they are a vast majority (86%).

In SAR observations, the average characteristic length scale L_{os} (Table 1) of the streaks varies between 1.1 and 1.2 km with standard deviations ranging from 0.3 to 0.8 km, which is substantial and can be attributed to the signal being noisy. The size of these streaks corresponds to the energy peaks at 0.9 km (Box East) and 1 km (Box West) in the energy spectra (black curves in Fig. 6d,f). The absence of energy peak at the km scale in Box South (Fig. 6e) is consistent with the fact that streaks are less frequent. In LESs, the average L_{os} is similar, ranging from 0.9 to 1.1 km in Boxes composed predominantly of streaks (Boxes East and South in Table 2). In Box West, this value is 1.5 km with a higher standard deviation (0.8 km). The energy peak found in LES (green curves in Fig. 6d) can be attributed to the presence of streaks in Box East. It is less pronounced in Box South (Fig. 6e), which contains only half as many streaks, and is absent in Box West (Fig. 6f), where streaks are scarce. The aspect ratio, i.e., the ratio between the length scale of the structures and the MABL height in LES, is comprised between 1.9–2.2 for Boxes East and South and 3.7 for Box West. The aspect ratio values are within the range (i.e., 2× z_i) observed in numerical studies (Weckwerth et al., 1997; Atkinson and Wu Zhang, 1996; Lfarh et al., 2024), but the larger aspect ratio in Box West suggests that the streaks are predominantly generated in the downstream portion of the domain. In SAR, the mean deviation of the streaks compared to the wind direction varies between 10-11° in Box West-South and 20° in Box East (see Table 1 and red dotted lines in Fig.8). This is within the large range of direction for boundary layer streaks seen by SAR observations (Etling and Brown, 1993). The LES reproduce the same range of observed deviation deviated counter-clockwise around +2 to +5 °. This difference in direction is, however, more pronounced than found in extratropical cyclones in Atkinson and Wu Zhang (1996); Lfarh et al. (2024).

https://doi.org/10.5194/egusphere-2026-3679
Preprint. Discussion started: 20 July 2026
© Author(s) 2026. CC BY 4.0 License.

To conclude, regions of high wind speed during Storm Alex are predominantly characterised by streak structures with a typical wavelength of approximately 1 km in SAR, aligned with the mean wind direction (Boxes East and West). The LES is able to reproduce these structures in Box East, whereas discrepancies arise in Box West between LES and observations. In Box South, both streaks and irregular patterns are also observed, and LES can reproduce these two distinct patterns. To further investigate the nature of these streaks and to explain the differences between SAR observations and LES results, an analysis of boundary layer processes is performed using the LES.

4.3 Vertical atmospheric structures in LES

Sea surface patterns are expected to be influenced by atmospheric processes (Vandemark et al., 2001). Surface streaks may originate from different mechanisms, including shear-driven surface-layer turbulence, boundary layer rolls, or gravity waves (Young et al., 2002). To characterise boundary layer circulations, vertical cross-sections are extracted from LES over subdomains where fine-scale structures are well resolved, along transects perpendicular to the mean wind direction (blue lines in Fig. 7b,d,f).

Figure 9 shows the corresponding vertical cross-sections. In Boxes East and South (a,b), where streaks are identified, alternating ascending and descending plumes are found, with approximately 10 updrafts in Box East and 9 in Box South, corresponding to a characteristic spacing ~ 1 km. These structures extend up to approximately 600 m in altitude, reaching or slightly exceeding the MABL top (dotted lines in Fig. 9). Maximum vertical velocities within updrafts and downdrafts reach approximately $\pm$ 2.5 $\mathrm{m\,s^{-1}}$. In contrast, the vertical cross-section in Box West (panel c), where no organised surface streaks are simulated, also exhibits ascending and descending motions, but these structures are (i) less organised, (ii) more intense, and (iii) extend to higher altitudes. They exceed the MABL top and interact with circulations in the free troposphere. Vertical velocities locally exceed $\pm$ 5 $\mathrm{m\,s^{-1}}$, with the strongest upward motions occurring within cloudy regions (blue contours in Fig. 9c).

Updrafts in Box East (a) are topped by shallow clouds extending vertically by 100 to 800 m. By contrast, Boxes South (b) and West (c) are characterised by more continuous cloud layers. The cloud layer is slightly thicker in Box West ($\sim$1500–2000 m) than in Box South ($\sim$1000-1500 m), due to a lower cloud base in Box W. Similarly, liquid water ratio (q_l) exceeds 1.6 $\mathrm{g\,kg^{-1}}$ in Box West, whereas it remains below 1 $\mathrm{g\,kg^{-1}}$ in Box South.

As shown in Fig. 5 (c,d), a LLJ (wind speed >25 $\mathrm{m\,s^{-1}}$, orange contours in Fig. 9) is present in all three Boxes. In Boxes East and South (Fig. 9 a,b), the LLJ is confined below 1 km altitude, whereas in Box West (panel c) it extends up to 2 km. Furthermore, the maximum LLJ intensity is stronger in Box West (37 $\mathrm{m\,s^{-1}}$, yellow contours) than in Box East (33 $\mathrm{m\,s^{-1}}$) and Box South (30 $\mathrm{m\,s^{-1}}$). Surface wind speeds are higher beneath downdrafts ($\sim$ 25 $\mathrm{m\,s^{-1}}$) than beneath ascending plumes (15–20 $\mathrm{m\,s^{-1}}$). These descending motions promote downward transport of LLJ momentum toward the surface. The resulting enhancement of near-surface wind speed locally increases both friction velocity and surface roughness.

The LES analysis suggests the presence of boundary layer rolls in Boxes East and South. This interpretation is supported by (i) the streak signatures identified from ACF analyses and (ii) the vertical cross-sections, which reveal updrafts and downdrafts occurring at regular intervals of approximately 1 km confined within the MABL. In addition, downdrafts appear associated with

https://doi.org/10.5194/egusphere-2026-3679
Preprint. Discussion started: 20 July 2026
© Author(s) 2026. CC BY 4.0 License.

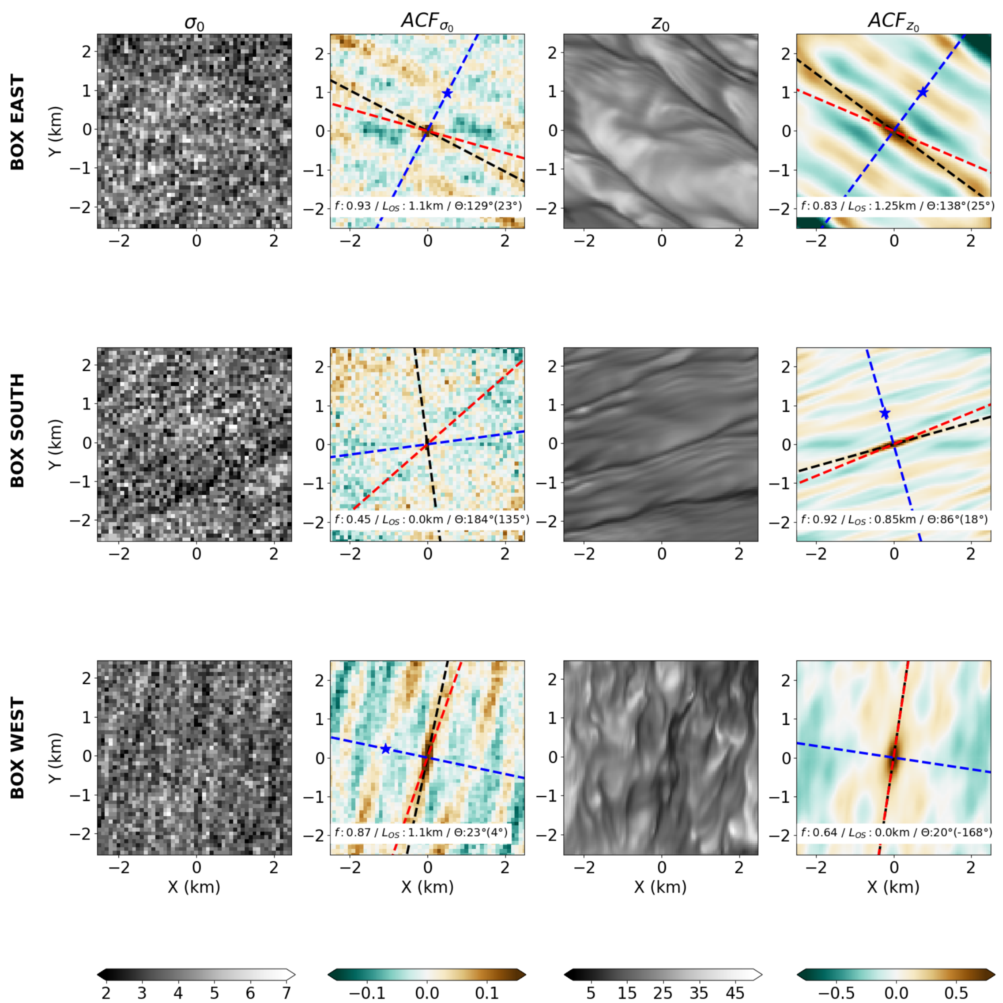

Figure 8. Spatial fields and corresponding two-dimensional autocorrelation functions (ACFs) for the three Boxes (EAST, SOUTH, and WEST). For each domain, the first column represents σ_0 (10^{-3} dB) and the second column displays its ACF (ACF_{σ_0}). The third column presents z_0 (10^{-4} m^{-1}) with its ACF (ACF_{z_0}) in the fourth column. The dashed black line indicates the orientation of the dominant correlation anisotropy (i.e., orientation of structures, degrees from north), while the red dashed line indicates the surface wind direction. The blue line indicates the perpendicular direction to the structure orientation where stars indicates the first peak of the corresponding one-dimensional autocorrelation. The labels at the bottom of each ACF panel (in brackets) report the anisotropy factor (or flatness) f, the characteristic length of structures L_{LOS}, and the orientation of structures Θ associated to the deviation with the surface wind.

enhanced surface winds through interactions with the LLJ, consistent with LLJ transport by boundary layer rolls proposed by Lfarh et al. (2023). By contrast, atmospheric structures in Box West cannot be interpreted as boundary layer rolls because they

https://doi.org/10.5194/egusphere-2026-3679
Preprint. Discussion started: 20 July 2026
© Author(s) 2026. CC BY 4.0 License.

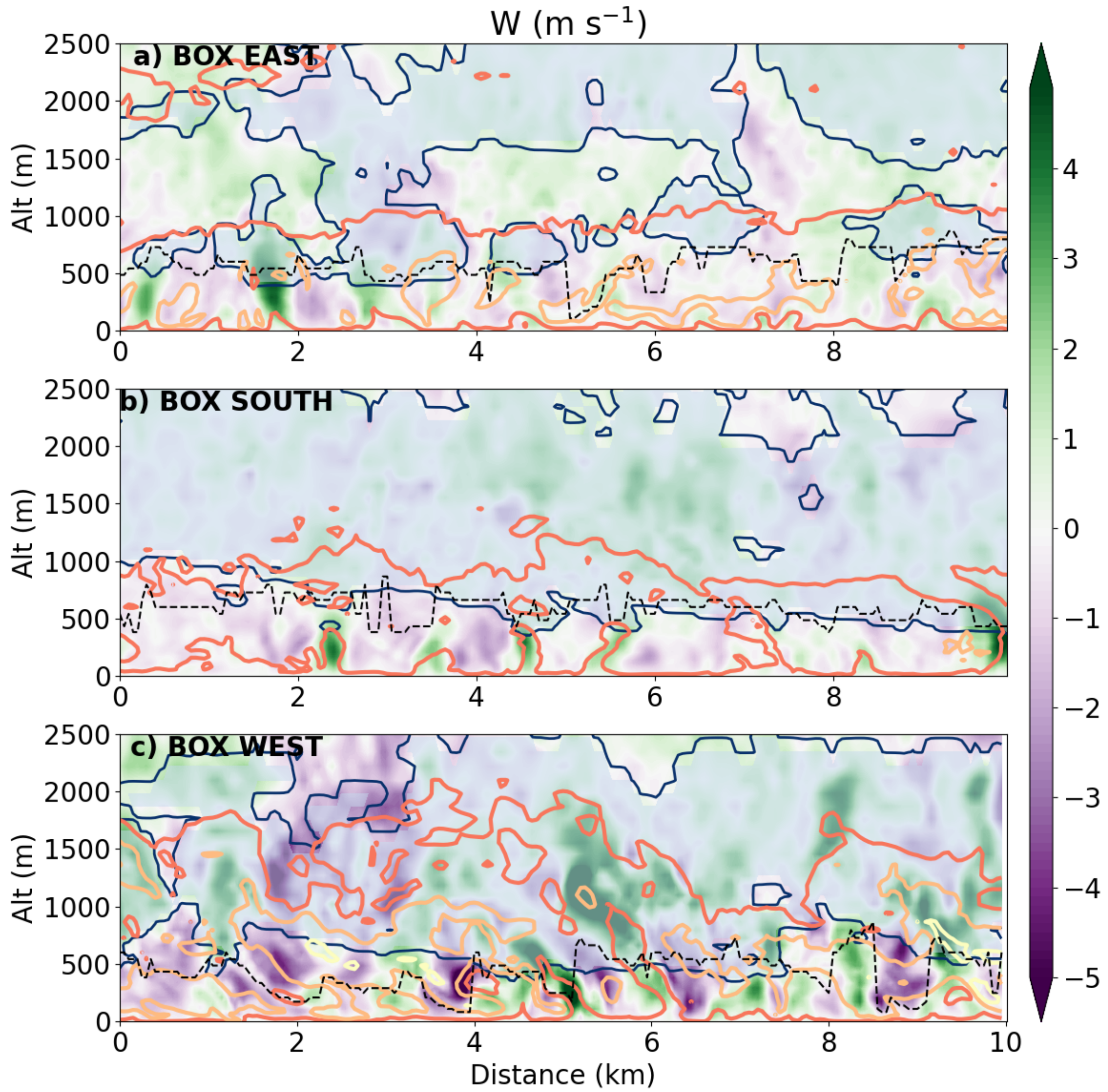

Figure 9. Vertical cross section of vertical velocity (shading) for Boxes a) East, b) South and c) West along the blue lines shown in Fig.7 (right panels). Dark orange, light orange and yellow bold contours represent 25, 30 and 35 $\mathrm{m\,s^{-1}}$ horizontal wind speed. Blue contours represent clouds ($q_l > 0.1$ g kg^{-1}). Dotted black lines represent the height of MABL.

extend beyond the MABL top and lack the linear organisation aligned with the mean wind direction. Their larger vertical extent and interaction with free-tropospheric circulations rather suggest a different dynamical regime. To investigate the absence of

https://doi.org/10.5194/egusphere-2026-3679
Preprint. Discussion started: 20 July 2026
© Author(s) 2026. CC BY 4.0 License.

boundary layer rolls in the LES over Box West, in contrast with observations, the following section examines the factors that may inhibit their development.

4.4 Factor controlling boundary layer rolls formation

This section focuses on the thermodynamic factors controlling the formation of boundary-layer rolls during Storm Alex. Previous studies, including (Etling and Brown, 1993; Moeng and Sullivan, 1994; Weckwerth et al., 1997), have investigated roll structures under a range of meteorological conditions and highlight the role of both thermal and dynamical instabilities as potential triggering mechanisms. Figure 10 compares the vertical profiles of static stability ($\frac{\partial \Theta}{\partial z}$), wind shear ($\frac{\partial U}{\partial z}$), and Richardson number (Ri; Eq. 4) across the subdomains in the vicinity of the vertical cross sections. The results reveal differences in boundary-layer structure, particularly between Boxes East and South and Box West, which respectively correspond to conditions with and without boundary layer rolls.

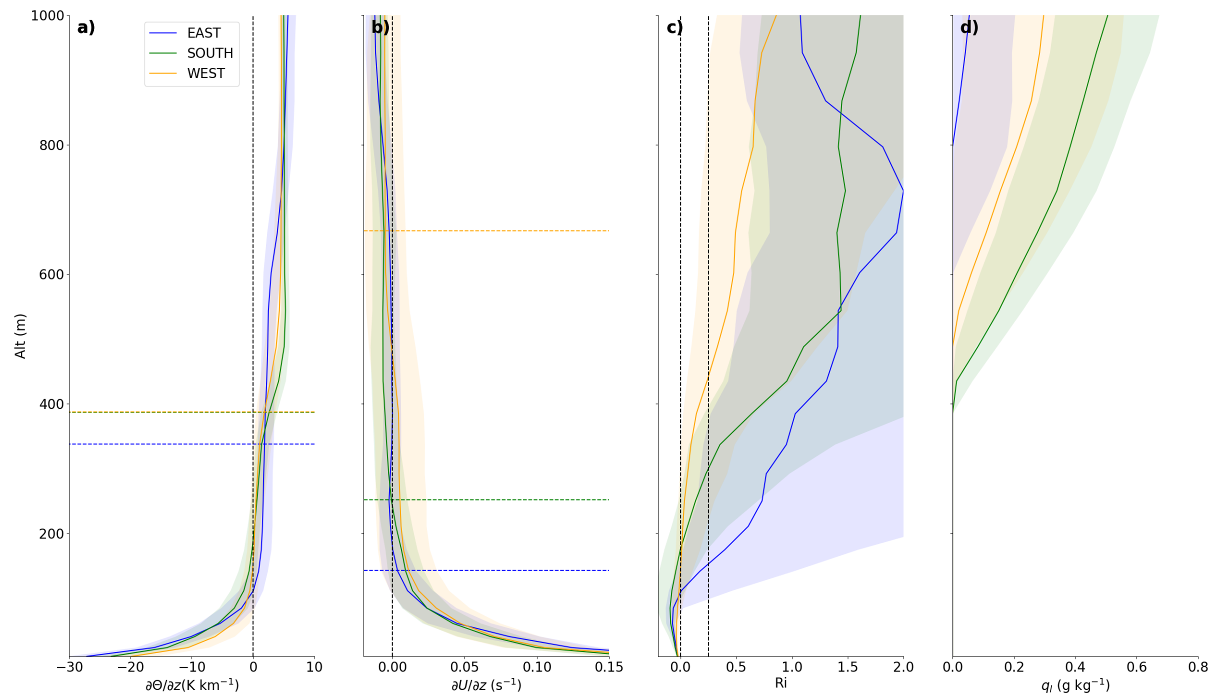

Figure 10. Vertical profiles of median vertical gradient of a) θ and b) wind, c) Richardson number Ri and d) liquid water ratio for Boxes East, South and West. Shaded areas correspond to the 25th and 75th percentile. The horizontal dotted lines correspond to a) the mean MABL top and b) the inflection point of wind.

The static stability (panel a) exhibits negative values near the surface in all Boxes, indicative of unstable MABL. However, Box West is less unstable near the surface compared to Box East (-20 versus -28 $\mathrm{K\,km^{-1}}$) but near-surface thermal instability alone is unlikely to explain the occurrence of boundary layer rolls (Weckwerth et al., 1997). Instead, the transition toward neutral or stable conditions occurs at different altitudes, reflecting contrasting MABL top. The MABL top is estimated with

https://doi.org/10.5194/egusphere-2026-3679
Preprint. Discussion started: 20 July 2026
© Author(s) 2026. CC BY 4.0 License.

Ri>0.25 from MNH800 (Fig. 5b) since Ri in LES is too noisy. It is equal to $\sim$ 340 m in Box East and $\sim$ 390 m in Boxes South and West (horizontal dotted lines in Fig. 10). The wind shear profiles (Fig. 10b) provide additional insight. All boxes exhibit a similar wind shear in the surface layer, around 0.15 s^{-1}, conditions sustaining boundary layer rolls establishment (Smedman, 1991; Alpers and Brümmer, 1994; Weckwerth et al., 1997; Santellanes et al., 2021). In Boxes East and South, wind shear decreases rapidly with altitude and becomes nearly zero above approximately 200 m, remaining weak throughout the MABL. This vertical homogenisation of momentum is consistent with the enhanced mixing induced by boundary layer rolls. In contrast, Box West exhibits persistent wind shear throughout the MABL, which can be related to the absence of roll structures. In addition, an inflection point within the MABL (horizontal dotted lines in panel (b)) is a necessary condition for the formation of boundary layer rolls (Alpers and Brümmer, 1994; Atkinson and Wu Zhang, 1996). In Boxes East and South, it is located within the MABL, whereas in Box West it lies above the top of the MABL. The Richardson number profiles (panel c) further highlight the contrasted atmospheric conditions among the three boxes. In Boxes East and South, Ri remains strongly negative throughout approximately half of the MABL before increasing and becoming positive, while still remaining below the critical Richardson number Ri=0.25 in the upper part of the MABL. Such a vertical profile is consistent with the presence of organised boundary layer rolls (Etling and Brown, 1993; Young et al., 2002). In contrast, Box West exhibits Ri values close to zero within the MABL, followed by a gradual increase with altitude over a thicker vertical extent. Finally, the cloud water content (panel d) does not indicate consistent differences between Box West and Boxes East and South. Thus, the model does not accurately represent the boundary layer rolls observed in Box West, because either the thermal instability is too weak or the wind shear is too strong, and this results in failing to organise into boundary layer rolls.

Surface fluxes play a key role in shaping the temperature profile and modulating thermal instability (Lfarh et al., 2024). Sensible (H) and latent (LE) heat fluxes are computed over the valid subdomains (see Table 1). Both H and LE reach their maximum values in Boxes East and South (approximately 265 and 400 $\mathrm{W\,m^{-2}}$, respectively), while Box West exhibits a lower values by about 30% and 27%. This contrast in H is primarily driven by the thermodynamic gradients controlling surface exchange processes, namely wind speed differences ($\Delta U = U_{10} - U_{\text{surface}}$ with $U_{\text{surface}} = 0$) and temperature contrast ($\Delta T =$ Temperature at 2 meters $-$ SST). The lower H in Box West is associated with a weaker ΔT (-2.5 K) compared to Boxes East and South (approximately -4 K). These three values of ΔT are comparable to those observed when boundary layer rolls are present (Brümmer and Wendel, 1987; Alpers and Brümmer, 1994; Atkinson and Wu Zhang, 1996). Although SST is relatively uniform across the three Boxes (around 290 K), temperature at 2 meters is higher in Box West than in the other two regions. Latent heat fluxes depends on both ΔU and the humidity contrast ΔHu (2 m relative humidity - 100%). Here again, ΔHu is less pronounced in Box West (16%) than in Boxes East and South (18.7–19.8%). While ΔU is larger in Box East than in Box West, potentially enhancing surface fluxes, the fluxes remain comparable between the two subdomains of Box South, suggesting that wind is not the primary controlling factor. According to Lfarh et al. (2024), a complete suppression of sensible heat fluxes inhibits the formation of boundary-layer rolls in LES of extratropical cyclone. Here, the reduction in total surface fluxes in Box West may provide a plausible explanation for the absence of boundary layer rolls by increasing the static stability close to the surface.

https://doi.org/10.5194/egusphere-2026-3679
Preprint. Discussion started: 20 July 2026
© Author(s) 2026. CC BY 4.0 License.

Box	H	LE	ΔT	ΔHu	ΔU
EAST	263±63	402±84	3.9±0.4	19.8±2.2	20.6±1.9
SOUTH-BLR	269± 53	396±66	4±0.2	18.7±1.4	14.9±4
WEST	184 ± 60	310±90	2.5±0.4	16.7±2.2	17.2±3.5

Table 2. Table of means and standard deviations for sensible and latent surface heat flux, difference between surface and first level of model for temperature, relative humidity and wind intensity in Boxes East, South and West.

5 Conclusion

This study combines C-band Synthetic Aperture Radar (SAR) observations from the Sentinel-1 satellite and Large-Eddy Simulations (LES) with the Meso-NH model to investigate the physical mechanisms controlling intense surface winds in Storm Alex during its warm seclusion phase over the English Channel on 2 Oct 2020. SAR provides unique high-resolution (100 m) snapshots of surface wind organisation, while LES allow investigating the associated boundary layer dynamics and fine-scale processes involved.

A first Meso-NH simulation at 800 m of horizontal grid spacing (MNH800), forced by the IFS operational analysis, reproduces the mesoscale structure of the storm, including the cold conveyor belt (CCB), warm sector, and the spatial distribution of the low-level jet (LLJ). Three distinct regions (labelled Box East, South, and West) of $\sim$ 50 x 50 km^2 where surface wind speed is high (> 25 $\mathrm{m\,s^{-1}}$) are simulated by using LES with 50 m of horizontal grid spacing. High surface wind speeds are associated to a LLJ located in the CCB of Storm Alex. The LLJ reaches approximately 30 $\mathrm{m\,s^{-1}}$ in Boxes East and South, where it extends from the surface to about 600 m, and up to 40 $\mathrm{m\,s^{-1}}$ in Box West, where it extends up to 1.5 km. A systematic underestimation of surface wind speed relative to SAR wind products is found in MNH800, and is not significantly reduced by increasing horizontal resolution, indicating that it likely arises from the IFS forcing and physical parameterisations including those for air–sea interaction processes rather than grid spacing alone. In the LESs, the simulated surface wind speed distribution becomes broader and exhibits more realistic extreme values with respect to SAR wind product, although the mean wind speed bias persists.

Energy spectra of SAR observations reveal enhanced energy at around 1 km wavelength in Boxes East and West while Box South displays a flatter spectral distribution. The LESs' spectral shapes match observations in Boxes East and South. The LES of Box West shows a markedly different behaviour, with a monotonic decrease in spectral energy toward smaller scales and no clear kilometre-scale peak, in disagreement with SAR data. To characterise the nature of the circulation responsible for the energy peaks, a two-dimensional autocorrelation function (ACF) is employed to identify the presence or absence of coherent structures and to quantify their characteristic spatial scales. The ACF is applied to the SAR backscatter coefficient (σ_0) and to the surface roughness length diagnosed from the LES. In SAR, the three boxes are characterised by streaks with typical scales of approximately 1.1 km and an alignment with the mean wind direction. The LES successfully reproduces the coherent structures observed by SAR in Boxes East and South. In contrast, in Box West, the autocorrelation analysis does not reveal streak-like structures in the LES, whereas such features are clearly predominant in the SAR observations.

https://doi.org/10.5194/egusphere-2026-3679
Preprint. Discussion started: 20 July 2026
© Author(s) 2026. CC BY 4.0 License.

Vertical cross-wind sections in Boxes East and South reveal quasi-periodic alternations of updrafts and downdrafts with a spacing of approximately 1 km. These structures are confined within the marine atmospheric boundary layer, with maximum vertical velocities of about $\pm$ 2–3 $\mathrm{m\,s^{-1}}$. They are consistent with boundary-layer rolls definition with a aspect ratio around 2 (Weckwerth et al., 1997). Surface winds are enhanced beneath their subsiding branches and LES analysis suggests that boundary-layer rolls act as a key organising mechanism for fine-scale wind structures in high-wind regions of Storm Alex, through efficient downward transport of momentum from LLJ. In contrast, Box West exhibits deeper and less organised vertical motions, with updrafts extending above the boundary layer top and interacting with the free troposphere. Vertical velocities exceed $\pm$ 5 $\mathrm{m\,s^{-1}}$ and are associated with a deeper cloud layer (up to 1.5–2 km). Stronger vertical wind shear and weaker surface buoyancy fluxes appear to inhibit the formation of organised boundary layer rolls in LES, leading instead to more disordered convective structures.

From a modelling point of view, this case study highlights the strong sensitivity of boundary layer rolls to the underlying thermodynamic and dynamical conditions of the atmosphere. In particular, the results suggest that their formation and organisation depend critically on vertical wind shear and thermal stability. Idealised LESs such as those presented by Wang and Jiang (2017) may help to systematically investigate the role of these controlling parameters. This study also shows that LESs are strongly influenced by lateral boundary conditions under strong wind regimes, and that a non-negligible fraction of the domain cannot be used to investigate fine-scale structures. Simulations performed over larger domains would (i) provide more robust statistics and (ii) allow the downstream evolution of advected boundary-layer rolls to be investigated. Recent advances in high-performance computing now make it feasible to run LES over 3D grids of up to one billion points becoming accessible (e.g., Escobar et al., 2025).

From an observational point of view, further investigation of surface coherent structures within high wind speed in extratropical cyclones could be done from Wave mode SAR acquisitions (with horizontal resolution $\sim$ 5 m) which provide significantly improved spatial resolution compared to the Interferometric Wide mode (100 m) images used here. Such data would help reduce the noise and sampling limitations when identifying fine-scale surface signatures, particularly under extreme wind conditions (Wang et al., 2019). However, the limited number of Wave mode SAR acquisitions, combined with their relatively small spatial coverage (20 × 20 $\mathrm{km^2}$), remains a significant constraint for systematic analyses of extratropical cyclone events, particularly when attempting to co-locate observations with high-resolution simulations.

Further progress will also benefit from coordinated field experiments combining in situ airborne measurements with SAR overpasses, especially under strong wind conditions associated with extratropical cyclone environments. Such measurements will provide direct constraints on fine-scale boundary layer turbulence and momentum transport processes that are otherwise difficult to infer from remote sensing alone. In this context, datasets from dedicated field campaigns represent a particularly valuable resource for investigating interactions between synoptic-scale forcing and boundary layer organisation. In February–March 2026, the dedicated NAWDIC-DICHOTOMI field campaign (Quinting et al., 2026; Rivière et al., 2026) deployed the ATR42 research aircraft in extratropical cyclones, equipped with two airborne Doppler radar systems: BASTA (Bistatic rAdar SysTem for Atmospheric observations; Delanoë et al. (2016)) and RASTA (RAdar SysTem Airborne). These instruments provide complementary measurements of the wind field within clouds and precipitation, enabling a detailed characterisation

https://doi.org/10.5194/egusphere-2026-3679
Preprint. Discussion started: 20 July 2026
© Author(s) 2026. CC BY 4.0 License.

of the vertical structure of winds from the surface to ~ 6 km with a spatial resolution. BASTA provides measurements with a temporal resolution of 0.1–1 s, corresponding to a spatial resolution of approximately 10–100 m, which offers a valuable opportunity for comparison with LES simulations.

Finally, this study highlights the potential of Synthetic Aperture Radar (SAR) observations to improve our understanding of complex fine-scale interactions within synoptic-scale systems. While boundary layer circulations in tropical cyclones have already been extensively investigated using SAR (Zhang et al., 2008; Foster, 2013; Wang et al., 2018), extending SAR analyses to hybrid systems such as medicanes (Miglietta et al., 2025) would help to better characterise local surface wind structures where tropical and extratropical features coexist (Colin and Husson, 2025; Avenas et al., 2026). Recent studies, such as Brumer et al. (2026) on Medicane Ianos, highlight that coupled ocean–atmosphere simulation provide a suitable framework to investigate how fine-scale air–sea interactions influence medicane wind structures and dynamics.

Author contributions. NM run the simulations, conducted the analysis of the data and wrote the paper with contributions of SEB, JP, AM, RH, and FP.

Competing interests. The authors declare that they have no conflict of interest.

Acknowledgements. The study was supported by the French National Research Agency under WINDGUST project (Grant ANR-21-CE01-0002) and European Space Agency under MEDICANES project (Contract No. 4000144111/23/I-KE). It was performed using HPC resources from GENCI-CINES (Grants gda2203 and lat0569 A0160111437). We acknowledge the French National Research Infrastructure CLIMERI-France https://climeri-france.fr/ which provides national label for the code Meso-NH. The authors thank Pierre-Etienne Brilouet (LEGOS) and Wahiba Lfarh (CNRM) for autocorrelation function discussion, Marie-Noëlle Bouin (CNRM) for spectral analysis discussion on SAR data and Marc Mandement (CNRM) for Météo-France weather stations and ground-based radar data.

https://doi.org/10.5194/egusphere-2026-3679
Preprint. Discussion started: 20 July 2026
© Author(s) 2026. CC BY 4.0 License.

References

Alpers, W. and Brümmer, B.: Atmospheric boundary layer rolls observed by the synthetic aperture radar aboard the ERS-1 satellite, Journal of Geophysical Research: Oceans, 99, 12 613–12 621, https://doi.org/10.1029/94JC00421, 1994.

Atkinson, B. W. and Wu Zhang, J.: Mesoscale shallow convection in the atmosphere, Reviews of Geophysics, 34, 403–431, https://doi.org/10.1029/96RG02623, https://agupubs.onlinelibrary.wiley.com/doi/abs/10.1029/96RG02623, 1996.

Avenas, A., Marcello Miglietta, M., Mouche, A., Dafis, S., Colin, A., Husson, R., and Flaounas, E.: Medicane characteristics from high-resolution satellite radar observations, Quarterly Journal of the Royal Meteorological Society, 152, e70 102, https://doi.org/https://doi.org/10.1002/qj.70102, https://rmets.onlinelibrary.wiley.com/doi/abs/10.1002/qj.70102, 2026.

Ayet, A., Rascle, N., Chapron, B., Couvreux, F., and Terray, L.: Uncovering air-sea interaction in oceanic submesoscale frontal regions using high-resolution satellite observations, US Clivar variations, 19, https://doi.org/10.5065/ybca-0s03, 2021.

Bador, M., Boé, J., Caillaud, C., Terray, L., Moine, M.-P., and Alias, A.: Cooler than observed sea surface could have reduced impacts of storm Alex and induced mediterranean heavy precipitation event in France, Climate Dynamics, 63, 460, https://doi.org/10.1007/s00382-025-07954-8, 2025.

Belamari, S.: Report on uncertainty estimates of an optimal bulk formulation for surface turbulent fluxes, Marine EnviRonment and Security for the European Area–Integrated Project (MERSEA IP), Deliverable D, 4, 505, 2005.

Blanchard, N., Pantillon, F., Chaboureau, J.-P., and Delanoë, J.: Organization of convective ascents in a warm conveyor belt, Weather and Climate Dynamics, 1, 617–634, https://doi.org/10.5194/wcd-1-617-2020, 2020.

Bougeault, P. and Lacarrere, P.: Parameterization of Orography-Induced Turbulence in a Mesobeta-Scale Model, Monthly Weather Review, 117, 1872–1890, https://doi.org/10.1175/1520-0493(1989)117<1872:POOITI>2.0.CO;2, 1989.

Bouin, M.-N., Lebeaupin Brossier, C., Malardel, S., Voldoire, A., and Sauvage, C.: The wave-age-dependent stress parameterisation (WASP) for momentum and heat turbulent fluxes at sea in SURFEX v8.1, Geoscientific Model Development, 17, 117–141, https://doi.org/10.5194/gmd-17-117-2024, 2024.

Brilouet, P.-E., Bouniol, D., Couvreux, F., Ayet, A., Granero-Belinchon, C., Lothon, M., and Mouche, A.: Trade Wind Boundary Layer Turbulence and Shallow Precipitating Convection: New Insights Combining SAR Images, Satellite Brightness Temperature, and Airborne In Situ Measurements, Geophysical Research Letters, 50, e2022GL102 180, https://doi.org/https://doi.org/10.1029/2022GL102180, https://agupubs.onlinelibrary.wiley.com/doi/abs/10.1029/2022GL102180, e2022GL102180 2022GL102180, 2023.

Brousseau, P., Seity, Y., Ricard, D., and Léger, J.: Improvement of the forecast of convective activity from the AROME-France system, Quarterly Journal of the Royal Meteorological Society, 142, 2231–2243, https://doi.org/https://doi.org/10.1002/qj.2822, https://rmets.onlinelibrary.wiley.com/doi/abs/10.1002/qj.2822, 2016.

Browning, K. A.: Organization of Clouds and Precipitation in Extratropical Cyclones, pp. 129–153, American Meteorological Society, Boston, MA, https://doi.org/10.1007/978-1-944970-33-8_8, https://doi.org/10.1007/978-1-944970-33-8_8, 1990.

Browning, K. A. and Field, M.: Evidence from Meteosat imagery of the interaction of sting jets with the boundary layer, Meteorological Applications, 11, 277–289, https://doi.org/https://doi.org/10.1017/S1350482704001379, https://rmets.onlinelibrary.wiley.com/doi/abs/10.1017/S1350482704001379, 2004.

Browning, K. A., Thorpe, A. J., Montani, A., Parsons, D., Griffiths, M., Panagi, P., and Dicks, E. M.: Interactions of Tropopause Depressions with an Ex–Tropical Cyclone and Sensitivity of Forecasts to Analysis Errors, Monthly Weather Review, 128, 2734

https://doi.org/10.5194/egusphere-2026-3679
Preprint. Discussion started: 20 July 2026
© Author(s) 2026. CC BY 4.0 License.

– 2755, https://doi.org/10.1175/1520-0493(2000)128<2734:IOTDWA>2.0.CO;2, https://journals.ametsoc.org/view/journals/mwre/128/8/1520-0493_2000_128_2734_iotdwa_2.0.co_2.xml, 2000.

Browning, K. A., Smart, D. J., Clark, M. R., and Illingworth, A. J.: The role of evaporating showers in the transfer of sting-jet momentum to the surface, Quarterly Journal of the Royal Meteorological Society, 141, 2956–2971, https://doi.org/10.1002/qj.2581, https://rmets.onlinelibrary.wiley.com/doi/abs/10.1002/qj.2581, 2015.

Brumer, S., Pantillon, F., Pianezze, J., and Maury, N.: Sub-mesoscale circulations and surface wave influence on strong winds in a mid-latitude cyclone, Weather and Climate Dynamics, -, –, https://doi.org/-, -, Submitted.

Brumer, S. E., Pantillon, F., Pianezze, J., Le Péru-Morvan, Y., Ragu-Fonta, M., Grand, L., Ricchi, A., Barboni, A., and Bouin, M.-N.: On the tropical nature of an intense Mediterranean cyclone in the ocean-atmosphere system, https://hal.science/hal-05444958, working paper or preprint, 2026.

Brümmer, B. and Wendel, M.: Observations of intermittent cumulus convection in the boundary layer, Quarterly Journal of the Royal Meteorological Society, 113, 19–36, https://doi.org/https://doi.org/10.1002/qj.49711347503, https://rmets.onlinelibrary.wiley.com/doi/abs/10.1002/qj.49711347503, 1987.

Carlson, T. N.: Airflow Through Midlatitude Cyclones and the Comma Cloud Pattern, Monthly Weather Review, 108, 1498 – 1509, https://doi.org/10.1175/1520-0493(1980)108<1498:ATMCAT>2.0.CO;2, https://journals.ametsoc.org/view/journals/mwre/108/10/1520-0493_1980_108_1498_atmcat_2_0_co_2.xml, 1980.

Chaboureau, J.-P. and Pinty, J.-P.: Validation of a cirrus parameterization with Meteosat Second Generation observations, Geophysical Research Letters, 33, https://doi.org/https://doi.org/10.1029/2005GL024725, https://agupubs.onlinelibrary.wiley.com/doi/abs/10.1029/2005GL024725, 2006.

Champeaux, J., Laurantin, O., Mercier, B., Mounier, F., Lassegues, P., and Tabary, P.: Quantitative precipitation estimations using rain gauges and radar networks: inventory and prospects at Meteo-France, in: WMO Joint Meeting of CGS Expert Team on Surface-based Remotely-sensed Observations and CIMO Expert Team on Operational Remote Sensing, vol. 5, pp. 1–11, 2011.

Chou, K.-H., Wu, C.-C., and Lin, S.-Z.: Assessment of the ASCAT wind error characteristics by global dropwindsonde observations, Journal of Geophysical Research (Atmospheres), 118, 9011–9021, https://doi.org/10.1002/jgrd.50724, 2013.

Colin, A. and Husson, R.: Rainfall regression from C-band synthetic aperture radar using multitask generative adversarial networks, Artificial Intelligence for the Earth Systems, 4, e240 007, 2025.

Cuxart, J., Bougeault, P., and Redelsperger, J.-L.: A turbulence scheme allowing for mesoscale and large-eddy simulations, Quarterly Journal of the Royal Meteorological Society, 126, 1–30, https://doi.org/https://doi.org/10.1002/qj.49712656202, https://rmets.onlinelibrary.wiley.com/doi/abs/10.1002/qj.49712656202, 2000.

Deardorff, J. W.: Stratocumulus-capped mixed layers derived from a three-dimensional model, Boundary-Layer Meteorology, 18, 495–527, https://doi.org/10.1007/BF00119502, 1980.

Delanoë, J., Protat, A., Vinson, J.-P., Brett, W., Caudoux, C., Bertrand, F., du Chatelet, J. P., Hallali, R., Barthes, L., Haeffelin, M., and Dupont, J.-C.: BASTA: A 95-GHz FMCW Doppler Radar for Cloud and Fog Studies, Journal of Atmospheric and Oceanic Technology, 33, 1023 – 1038, https://doi.org/10.1175/JTECH-D-15-0104.1, https://journals.ametsoc.org/view/journals/atot/33/5/jtech-d-15-0104_1.xml, 2016.

Eisenstein, L., Pantillon, F., and Knippertz, P.: Dynamics of sting-jet storm Egon over continental Europe: Impact of surface properties and model resolution, Quarterly Journal of the Royal Meteorological Society, 146, 186–210, https://doi.org/10.1002/qj.3666, https://rmets.onlinelibrary.wiley.com/doi/abs/10.1002/qj.3666, 2020.

Escobar, J., Wautelet, P., Pianezze, J., Pantillon, F., Dauhut, T., Barthe, C., and Chaboureau, J.-P.: Porting the Meso-NH atmospheric model on different GPU architectures for the next generation of supercomputers (version MESONH-v55-OpenACC), Geoscientific Model Development, 18, 2679–2700, https://doi.org/10.5194/gmd-18-2679-2025, https://gmd.copernicus.org/articles/18/2679/2025/, 2025.

Etling, D. and Brown, R. A.: Roll vortices in the planetary boundary layer: A review, Boundary-Layer Meteorology, 65, 215–248, https://doi.org/10.1007/BF00705527, 1993.

Fairall, C. W., Bradley, E. F., Rogers, D. P., Edson, J. B., and Young, G. S.: Bulk parameterization of air-sea fluxes for tropical ocean-global atmosphere coupled-ocean atmosphere response experiment, Journal of Geophysical Research: Oceans, 101, 3747–3764, https://doi.org/10.1029/95JC03205, 1996.

Figa-Saldana, J., Wilson, J. J. W., Attema, E; Gelsthorpe, R., Drinkwater, M. R., and Stofflen, A.: The advanced scatterometer (ASCAT) on the meteorological operational (MetOp) platform: A follow on for European wind scatterometers, Canadian journal of remote sensing, https://doi.org/10.5589/m02-035, 2002.

Figueras i Ventura, J. and Tabary, P.: The New French Operational Polarimetric Radar Rainfall Rate Product, Journal of Applied Meteorology and Climatology, 52, 1817 – 1835, https://doi.org/10.1175/JAMC-D-12-0179.1, https://journals.ametsoc.org/view/journals/apme/52/8/jamc-d-12-0179.1.xml, 2013.

Foster, R. C.: Signature of large aspect ratio roll vortices in synthetic aperture radar images of tropical cyclones, Oceanography, 26, 58–67, https://doi.org/10.5670/oceanog.2013.31, 2013.

Fu, L.-L.: Seasat views oceans and sea ice with synthetic-aperture radar, vol. 81, California Institute of Technology, Jet Propulsion Laboratory, 1982.

Gentile, E. S. and Gray, S. L.: Attribution of observed extreme marine wind speeds and associated hazards to midlatitude cyclone conveyor belt jets near the British Isles, International Journal of Climatology, 43, 2735–2753, https://doi.org/https://doi.org/10.1002/joc.7999, https://rmets.onlinelibrary.wiley.com/doi/abs/10.1002/joc.7999, 2023.

Ginesta, M., Flaounas, E., Yiou, P., and Faranda, D.: Anthropogenic Climate Change Will Intensify European Explosive Storms Analogous to Alex, Eunice, and Xynthia, Journal of Climate, 37, 5427 – 5452, https://doi.org/10.1175/JCLI-D-23-0761.1, https://journals.ametsoc.org/view/journals/clim/37/21/JCLI-D-23-0761.1.xml, 2024.

Giraldo, C. and Le Roy, D.: CGFS2020 cruise, RV Thalassa, https://doi.org/10.17600/18000675, 2020.

Granero Belinchon, C., Roux, S. G., Garnier, N. B., Tandeo, P., Chapron, B., and Mouche, A.: Two-dimensional structure functions for characterizing convective rolls in the marine atmospheric boundary layer from Sentinel-1 SAR images, Remote Sensing Letters, 13, 946–957, https://doi.org/10.1080/2150704X.2022.2112107, https://doi.org/10.1080/2150704X.2022.2112107, 2022.

Harvey, B., Methven, J., Eagle, C., and Lean, H.: Does the Representation of Flow Structure and Turbulence at a Cold Front Converge on Multiscale Observations with Model Resolution?, Monthly Weather Review, 145, 4345 – 4363, https://doi.org/10.1175/MWR-D-16-0479.1, https://journals.ametsoc.org/view/journals/mwre/145/11/mwr-d-16-0479.1.xml, 2017.

Hewson, T. D. and Neu, U.: Cyclones, windstorms and the IMILAST project, Tellus A: Dynamic Meteorology and Oceanography, 67, 27 128, https://doi.org/10.3402/tellusa.v67.27128, 2015.

Hobbs, P. V.: Organization and structure of clouds and precipitation on the mesoscale and microscale in cyclonic storms, Reviews of Geophysics, 16, 741–755, https://doi.org/https://doi.org/10.1029/RG016i004p00741, https://agupubs.onlinelibrary.wiley.com/doi/abs/10.1029/RG016i004p00741, 1978.

https://doi.org/10.5194/egusphere-2026-3679
Preprint. Discussion started: 20 July 2026
© Author(s) 2026. CC BY 4.0 License.

Huang, L., Li, X., Liu, B., Zhang, J. A., Shen, D., Zhang, Z., and Yu, W.: Tropical Cyclone Boundary Layer Rolls in Synthetic Aperture Radar Imagery, Journal of Geophysical Research: Oceans, 123, 2981–2996, https://doi.org/https://doi.org/10.1029/2018JC013755, https://agupubs.onlinelibrary.wiley.com/doi/abs/10.1029/2018JC013755, 2018.

Kudryavtsev, V., Akimov, D., Johannessen, J., and Chapron, B.: On radar imaging of current features: 1. Model and comparison with observations, Journal of Geophysical Research: Oceans, 110, https://doi.org/10.1029/2004JC002505, 2005.

Lac, C., Chaboureau, J.-P., Masson, V., Pinty, J.-P., Tulet, P., Escobar, J., Leriche, M., Barthe, C., Aouizerats, B., Augros, C., Aumond, P., Auguste, F., Bechtold, P., Berthet, S., Bielli, S., Bosseur, F., Caumont, O., Cohard, J.-M., Colin, J., Couvreux, F., Cuxart, J., Delautier, G., Dauhut, T., Ducrocq, V., Filippi, J.-B., Gazen, D., Geoffroy, O., Gheusi, F., Honnert, R., Lafore, J.-P., Lebeaupin Brossier, C., Libois, Q., Lunet, T., Mari, C., Maric, T., Mascart, P., Mogé, M., Molinié, G., Nuissier, O., Pantillon, F., Peyrillé, P., Pergaud, J., Perraud, E., Pianezze, J., Redelsperger, J.-L., Ricard, D., Richard, E., Riette, S., Rodier, Q., Schoetter, R., Seyfried, L., Stein, J., Suhre, K., Taufour, M., Thouron, O., Turner, S., Verrelle, A., Vié, B., Visentin, F., Vionnet, V., and Wautelet, P.: Overview of the Meso-NH model version 5.4 and its applications, Geoscientific Model Development, 11, 1929–1969, https://doi.org/10.5194/gmd-11-1929-2018, https://www.geosci-model-dev.net/11/1929/2018/, 2018.

Levy, G.: Boundary layer roll statistics from SAR, Geophysical Research Letters, 28, 1993–1995, https://doi.org/10.1029/2000GL012667, 2001.

Lfarh, W., Pantillon, F., and Chaboureau, J.-P.: The Downward Transport of Strong Wind by Convective Rolls in a Mediterranean Windstorm, Monthly Weather Review, 151, 2801 – 2817, https://doi.org/10.1175/MWR-D-23-0099.1, https://journals.ametsoc.org/view/journals/mwre/151/10/MWR-D-23-0099.1.xml, 2023.

Lfarh, W., Pantillon, F., Chaboureau, J.-P., and Brumer, S. E.: Impact of Surface Turbulent Fluxes on the Formation of Roll Vortices in a Mediterranean Windstorm, Journal of Geophysical Research: Atmospheres, 129, e2023JD040 191, https://doi.org/https://doi.org/10.1029/2023JD040191, https://agupubs.onlinelibrary.wiley.com/doi/abs/10.1029/2023JD040191, e2023JD040191 2023JD040191, 2024.

Li, X., Pu, Z., and Gao, Z.: Effects of Roll Vortices on the Evolution of Hurricane Harvey during Landfall, Journal of the Atmospheric Sciences, 78, 1847 – 1867, https://doi.org/10.1175/JAS-D-20-0270.1, https://journals.ametsoc.org/view/journals/atsc/78/6/JAS-D-20-0270.1.xml, 2021.

Lohou, F., Campistron, B., Druilhet, A., Foster, P., and Pages, J.: Turbulence and coherent organizations in the atmospheric boundary layer: A radar-aircraft experimental approach, Boundary-layer meteorology, 86, 147–179, https://doi.org/10.1023/A:1000613232592, 1998.

Martins, C., Piton, G., Kuss, D., Guitet, C., Carladous, S., Robert, Y., Andréis, N., Liébault, F., Chapuis, M., Passy, P., Melun, G., Misset, C., and Quefféléan, Y.: Tempête Alex – retour d'expérience des crues torrentielles du 2 octobre 2020 dans les Alpes-Maritimes, LHB, 110, 2381 471, https://doi.org/10.1080/27678490.2024.2381471, https://doi.org/10.1080/27678490.2024.2381471, 2024.

Martínez-Alvarado, O., Gray, S. L., Hart, N. C. G., Clark, P. A., Hodges, K., and Roberts, M. J.: Increased wind risk from sting-jet windstorms with climate change, Environmental Research Letters, 13, 044 002, https://doi.org/10.1088/1748-9326/aaae3a, https://dx.doi.org/10.1088/1748-9326/aaae3a, 2018.

Masson, V., Le Moigne, P., Martin, E., Faroux, S., Alias, A., Alkama, R., Belamari, S., Barbu, A., Boone, A., Bouyssel, F., Brousseau, P., Brun, E., Calvet, J.-C., Carrer, D., Decharme, B., Delire, C., Donier, S., Essaouini, K., Gibelin, A.-L., Giordani, H., Habets, F., Jidane, M., Kerdraon, G., Kourzeneva, E., Lafaysse, M., Lafont, S., Lebeaupin Brossier, C., Lemonsu, A., Mahfouf, J.-F., Marguinaud, P., Mokhtari, M., Morin, S., Pigeon, G., Salgado, R., Seity, Y., Taillefer, F., Tanguy, G., Tulet, P., Vincendon, B., Vionnet, V., and Voldoire, A.: The

https://doi.org/10.5194/egusphere-2026-3679
Preprint. Discussion started: 20 July 2026
© Author(s) 2026. CC BY 4.0 License.

SURFEXv7.2 land and ocean surface platform for coupled or offline simulation of Earth surface variables and fluxes, Geoscientific Model Development, 6, 929–960, https://doi.org/10.5194/gmd-6-929-2013, https://gmd.copernicus.org/articles/6/929/2013/, 2013.

Miglietta, M. M., Flaounas, E., González-Alemán, J. J., Panegrossi, G., Gaertner, M. A., Pantillon, F., Pasquero, C., Schultz, D. M., D'Adderio, L. P., Dafis, S., Husson, R., Ricchi, A., Carrió, D. S. C., Davolio, S., Fita, L., Ángeles Picornell, M., Pytharoulis, I., Raveh-Rubin, S., Scoccimarro, E., Bernini, L., Cavicchia, L., Conte, D., Ferretti, R., Flocas, H., Gutiérrez-Fernández, J., Hatzaki, M., Santaner, V. H., Jansà, A., and Patlakas, P.: Defining Medicanes: Bridging the Knowledge Gap between Tropical and Extratropical Cyclones in the Mediterranean, Bulletin of the American Meteorological Society, 106, E1955 – E1971, https://doi.org/10.1175/BAMS-D-24-0289.1, https://journals.ametsoc.org/view/journals/bams/106/9/BAMS-D-24-0289.1.xml, 2025.

Moeng, C.-H. and Sullivan, P. P.: A Comparison of Shear- and Buoyancy-Driven Planetary Boundary Layer Flows, Journal of Atmospheric Sciences, 51, 999 – 1022, https://doi.org/10.1175/1520-0469(1994)051<0999:ACOSAB>2.0.CO;2, https://journals.ametsoc.org/view/journals/atsc/51/7/1520-0469_1994_051_0999_acosab_2_0_co_2.xml, 1994.

Monin, A. S. and Obukhov, A. M.: Basic laws of turbulent mixing in the surface layer of the atmosphere, Contrib. Geophys. Inst. Acad. Sci. USSR, 151, e187, 1954.

Mouche, A., Chapron, B., Knaff, J., Zhao, Y., Zhang, B., and Combot, C.: Copolarized and cross-polarized SAR measurements for high-resolution description of major hurricane wind structures: Application to Irma category 5 hurricane, Journal of Geophysical Research: Oceans, 124, 3905–3922, https://doi.org/10.1029/2019JC015056, 2019.

Mouche, A. A., Chapron, B., Zhang, B., and Husson, R.: Combined co-and cross-polarized SAR measurements under extreme wind conditions, IEEE Transactions on Geoscience and Remote Sensing, 55, 6746–6755, https://doi.org/10.1109/TGRS.2017.2732508, 2017.

Mourad, P., Thompson, D., and Vandemark, D.: Extracting Fine-Scale Wind Fields from Synthetic Aperture Radar Images of the Ocean Surface, Johns Hopkins Apl Technical Digest, 21, 108–115, 2000.

Neu, U., Akperov, M., Bellenbaum, N., Benestad, R., Blender, R., Caballero, R., Cocozza, A., Dacre, H., Feng, Y., Fraedrich, K., Grieger, J., Gulev, S., Hanley, J., Hewson, T., Inatsu, M., Keay, K., Kew, S., Kindem, I., Leckebusch, G., and Wernli, H.: IMILAST: A Community Effort to Intercompare Extratropical Cyclone Detection and Tracking Algorithms, Bulletin of the American Meteorological Society, 94, 529–547, https://doi.org/10.1175/BAMS-D-11-00154.1, 2013.

Pantillon, F., Adler, B., Corsmeier, U., Knippertz, P., Wieser, A., and Hansen, A.: Formation of Wind Gusts in an Extratropical Cyclone in Light of Doppler Lidar Observations and Large-Eddy Simulations, Monthly Weather Review, 148, 353 – 375, https://doi.org/10.1175/MWR-D-19-0241.1, https://journals.ametsoc.org/view/journals/mwre/148/1/mwr-d-19-0241.1.xml, 2020.

Parton, G., Vaughan, G., Norton, E., Browning, K., and Clark, P.: Wind profiler observations of a sting jet, Quarterly Journal of The Royal Meteorological Society - QUART J ROY METEOROL SOC, 135, 663–680, https://doi.org/10.1002/qj.398, 2009.

Parton, G., Dore, A., and Vaughan, G.: A climatology of mid-tropospheric mesoscale strong wind events as observed by the MST radar, Aberystwyth, Meteorological Applications, 17, 340–354, https://doi.org/https://doi.org/10.1002/met.203, https://rmets.onlinelibrary.wiley.com/doi/abs/10.1002/met.203, 2010.

Pergaud, J., Masson, V., Malardel, S., and Couvreux, F.: A Parameterization of Dry Thermals and Shallow Cumuli for Mesoscale Numerical Weather Prediction, Boundary-Layer Meteorology, 132, 83–106, https://doi.org/10.1007/s10546-009-9388-0, 2009.

Pineau-Guillou, L., Ardhuin, F., Bouin, M.-N., Redelsperger, J.-L., Chapron, B., Bidlot, J.-R., and Quilfen, Y.: Strong winds in a coupled wave–atmosphere model during a North Atlantic storm event: evaluation against observations, Quarterly Journal of the Royal Meteorological Society, 144, 317–332, https://doi.org/https://doi.org/10.1002/qj.3205, https://rmets.onlinelibrary.wiley.com/doi/abs/10.1002/qj.3205, 2018.

© Author(s) 2026. CC BY 4.0 License.

Pinty, J.-P. and Jabouille, P.: A mixed-phase cloud parameterization for use in a mesoscale non-hydrostatic model: simulations of a squall line and of orographic precipitations, in: Conf. on cloud physics, pp. 217–220, Amer. Meteor. Soc., Everett, WA, 1998.

Polverari, F., Portabella, M., Lin, W., Sapp, J. W., Stoffelen, A., Jelenak, Z., and Chang, P. S.: On high and extreme wind calibration using ASCAT, IEEE Transactions on Geoscience and Remote Sensing, 60, 1–10, https://doi.org/10.1109/TGRS.2021.3079898, 2021.

Quinting, J., Grams, C. M., Kirsch, B., Oertel, A., Ramos, A. M., Raveh-Rubin, S., and Schäfler, A.: Dry intrusion connects high-impact cyclones Eunice and Franklin: emerging observational targets of NAWDIC, Bulletin of the American Meteorological Society, pp. BAMS–D–25–0170.1, https://doi.org/10.1175/BAMS-D-25-0170.1, https://journals.ametsoc.org/view/journals/bams/aop/BAMS-D-25-0170.1/BAMS-D-25-0170.1.xml, 2026.

Raveh-Rubin, S.: Dry Intrusions: Lagrangian Climatology and Dynamical Impact on the Planetary Boundary Layer, Journal of Climate, 30, 6661 – 6682, https://doi.org/10.1175/JCLI-D-16-0782.1, https://journals.ametsoc.org/view/journals/clim/30/17/jcli-d-16-0782.1.xml, 2017.

Rivière, G., Delanoë, J., Pantillon, F., Ricard, D., Planche, C., Coutris, P., and Sodemann, H.: La campagne Nawdic sur les tempêtes hivernales, La Météorologie, 2026, 4–7, 2026.

Rivière, G., Ricard, D., and Arbogast, P.: The downward transport of momentum to the surface in idealized sting-jet cyclones, Quarterly Journal of the Royal Meteorological Society, 146, 1801–1821, https://doi.org/https://doi.org/10.1002/qj.3767, https://rmets.onlinelibrary.wiley.com/doi/abs/10.1002/qj.3767, 2020.

Sanders, F. and Gyakum, J. R.: Synoptic-Dynamic Climatology of the “Bomb”, Monthly Weather Review, 108, 1589 – 1606, https://doi.org/10.1175/1520-0493(1980)108<1589:SDCOT>2.0.CO;2, https://journals.ametsoc.org/view/journals/mwre/108/10/1520-0493_1980_108_1589_sdcot_2_0_co_2.xml, 1980.

Santellanes, S. R., Young, G. S., Stensrud, D. J., Kumjian, M. R., and Pan, Y.: Environmental Conditions Associated with Horizontal Convective Rolls, Cellular Convection, and No Organized Circulations, Monthly Weather Review, 149, 1305 – 1316, https://doi.org/10.1175/MWR-D-20-0207.1, https://journals.ametsoc.org/view/journals/mwre/149/5/MWR-D-20-0207.1.xml, 2021.

Saunders, R., Hocking, J., Turner, E., Rayer, P., Rundle, D., Brunel, P., Vidot, J., Roquet, P., Matricardi, M., Geer, A., Bormann, N., and Lupu, C.: An update on the RTTOV fast radiative transfer model (currently at version 12), Geoscientific Model Development, 11, 2717–2737, https://doi.org/10.5194/gmd-11-2717-2018, https://gmd.copernicus.org/articles/11/2717/2018/, 2018.

Schultz, D. M., Bosart, L. F., Colle, B. A., Davies, H. C., Dearden, C., Keyser, D., Martius, O., Roebber, P. J., Steenburgh, W. J., Volkert, H., and Winters, A. C.: Extratropical Cyclones: A Century of Research on Meteorology's Centerpiece, Meteorological Monographs, 59, 16.1 – 16.56, https://doi.org/10.1175/AMSMONOGRAPHS-D-18-0015.1, https://journals.ametsoc.org/view/journals/amsm/59/1/amsmonographs-d-18-0015.1.xml, 2019.

Seity, Y., Brousseau, P., Malardel, S., Hello, G., Bénard, P., Bouttier, F., Lac, C., and Masson, V.: The AROME-France convective-scale operational model, Monthly Weather Review, 139, 976–991, https://doi.org/10.1175/2010MWR3425.1, 2011.

Shapiro, M., Wernli, H., Bao, J.-W., Methven, J., Zou, X., Doyle, J., Holt, T., Donall-Grell, E., and Neiman, P.: A Planetary-Scale to Mesoscale Perspective of the Life Cycles of Extratropical Cyclones: The Bridge between Theory and Observations, pp. 139–185, American Meteorological Society, Boston, MA, https://doi.org/10.1007/978-1-935704-09-6_14, https://doi.org/10.1007/978-1-935704-09-6_14, 1999.

Shapiro, M. A. and Keyser, D.: Fronts, Jet Streams and the Tropopause, pp. 167–191, American Meteorological Society, Boston, MA, https://doi.org/10.1007/978-1-944970-33-8_10, https://doi.org/10.1007/978-1-944970-33-8_10, 1990.

https://doi.org/10.5194/egusphere-2026-3679
Preprint. Discussion started: 20 July 2026
© Author(s) 2026. CC BY 4.0 License.

Sikora, T. D. and Ufermann, S.: Synthetic Aperture Radar Signatures of Marine Atmospheric Boundary Layer Cellular Convection and Longitudinal Roll Vortices, in: SAR Marine User's Manual, edited by Apel, J. and Jackson, C., pp. 321–330, NOAA/NESDIS, 2004.

Smedman, A.-S.: Occurrence of roll circulations in a shallow boundary layer, Boundary-Layer Meteorology, 57, 343–358, 1991.

Stopa, J. E., Wang, C., Vandemark, D., Foster, R., Mouche, A., and Chapron, B.: Automated Global Classification of Surface Layer Stratification Using High-Resolution Sea Surface Roughness Measurements by Satellite Synthetic Aperture Radar, Geophysical Research Letters, 49, e2022GL098 686, https://doi.org/https://doi.org/10.1029/2022GL098686, https://agupubs.onlinelibrary.wiley.com/doi/abs/10.1029/2022GL098686, e2022GL098686 2022GL098686, 2022.

Thompson, T. W., Liu, W. T., and Weissman, D. E.: Synthetic aperture radar observation of ocean roughness from rolls in an unstable marine boundary layer, Geophysical Research Letters, 10, 1172–1175, https://doi.org/10.1029/GL010i012p01172, 1983.

Valenzuela, G.: Depolarization of EM waves by slightly rough surfaces, IEEE Transactions on Antennas and Propagation, 15, 552–557, https://doi.org/10.1109/TAP.1967.1138962, 1967.

Valenzuela, G. R.: Theories for the interaction of electromagnetic and oceanic waves—A review, Boundary-Layer Meteorology, 13, 61–85, https://doi.org/10.1007/BF00913863, 1978.

Vandemark, D., Mourad, P. D., Bailey, S. A., Crawford, T. L., Vogel, C. A., Sun, J., and Chapron, B.: Measured changes in ocean surface roughness due to atmospheric boundary layer rolls, Journal of Geophysical Research: Oceans, 106, 4639–4654, https://doi.org/10.1029/1999JC000051, https://agupubs.onlinelibrary.wiley.com/doi/abs/10.1029/1999JC000051, 2001.

Voronovich, A. G. and Zavorotny, V. U.: Full-polarization modeling of monostatic and bistatic radar scattering from a rough sea surface, IEEE Transactions on Antennas and Propagation, 62, 1362–1371, https://doi.org/10.1109/TAP.2013.2295235, 2013.

Wang, C., Mouche, A., Foster, R. C., Vandemark, D., and Chapron, B.: Tropical cyclone boundary layer rolls in Sentinel-1 SAR imagery, Journal of Geophysical Research: Oceans, 123, 2981–2996, https://doi.org/10.1029/2018JC013755, 2018.

Wang, C., Mouche, A., Foster, R. C., Vandemark, D., Stopa, J. E., Tandeo, P., Longépé, N., and Chapron, B.: Characteristics of Marine Atmospheric Boundary Layer Roll Vortices from Sentinel-1 SAR Wave Mode, in: IEEE International Geoscience and Remote Sensing Symposium (IGARSS), pp. 7908–7911, https://doi.org/10.1109/IGARSS.2019.8900287, 2019.

Wang, C., Vandemark, D., Mouche, A., Chapron, B., Li, H., and Foster, R. C.: An assessment of marine atmospheric boundary layer roll detection using Sentinel-1 SAR data, Remote Sensing of Environment, 250, 112 031, https://doi.org/10.1016/j.rse.2020.112031, 2020.

Wang, C., Stopa, J. E., Vandemark, D., Foster, R., Ayet, A., Mouche, A., Chapron, B., and Sadowski, P.: A multi-tagged SAR ocean image dataset identifying atmospheric boundary layer structure in winter tradewind conditions, Geoscience Data Journal, 12, e282, https://doi.org/https://doi.org/10.1002/gdj3.282, https://rmets.onlinelibrary.wiley.com/doi/abs/10.1002/gdj3.282, e282 GDJ-2023-06-0027.R2, 2025.

Wang, S. and Jiang, Q.: Impact of vertical wind shear on roll structure in idealized hurricane boundary layers, Atmospheric Chemistry and Physics, 17, 3507–3524, https://doi.org/10.5194/acp-17-3507-2017, https://acp.copernicus.org/articles/17/3507/2017/, 2017.

Weckwerth, T. M., Wilson, J. W., Wakimoto, R. M., and Crook, N. A.: Horizontal convective rolls: Determining the environmental conditions supporting their existence and characteristics, Monthly weather review, 125, 505–526, 1997.

Young, G. S., Kristovich, D. A., Hjelmfelt, M. R., and Foster, R. C.: Rolls, streets, waves, and more: A review of quasi-two-dimensional structures in the atmospheric boundary layer, Bulletin of the American Meteorological Society, 83, 997–1002, 2002.

Zhang, J. A., Katsaros, K. B., Black, P. G., Lehner, S., French, J. R., and Drennan, W. M.: Effects of roll vortices on turbulent fluxes in the hurricane boundary layer, Boundary-layer meteorology, 128, 173–189, https://doi.org/10.1007/s10546-008-9281-2, 2008.